A network of assembly factors is involved in remodeling rRNA elements during preribosome maturation

Jochen Baßler,[1]* Helge Paternoga,[1]* Iris Holdermann,[1] Matthias Thoms,[1] Sander Granneman,[2] Clara Barrio-Garcia,[4] Afua Nyarko,[5] Gunter Stier,[1] Sarah A. Clark,[5] Daniel Schraivogel,[1] Martina Kallas,[1] Roland Beckmann,[4] David Tollervey,[3] Elisar Barbar,[5]** Irmi Sinning,[1]** and Ed Hurt[1]**

[1]Biochemistry Center of Heidelberg University, INF328, D-69120 Heidelberg, Germany
[2]Centre for Synthetic and Systems Biology (SynthSys) and [3]Wellcome Trust Centre for Cell Biology, University of Edinburgh, Edinburgh EH9 3BF, Scotland, UK
[4]Gene Center, Department of Chemistry and Biochemistry, University of Munich, 80539 Munich, Germany
[5]Department of Biochemistry and Biophysics, Oregon State University, Corvallis, OR 97331

Eukaryotic ribosome biogenesis involves ∼200 assembly factors, but how these contribute to ribosome maturation is poorly understood. Here, we identify a network of factors on the nascent 60S subunit that actively remodels preribosome structure. At its hub is Rsa4, a direct substrate of the force-generating ATPase Rea1. We show that Rsa4 is connected to the central protuberance by binding to Rpl5 and to ribosomal RNA (rRNA) helix 89 of the nascent peptidyl transferase center (PTC) through Nsa2. Importantly, Nsa2 binds to helix 89 before relocation of helix 89 to the PTC. Structure-based mutations of these factors reveal the functional importance of their interactions for ribosome assembly. Thus, Rsa4 is held tightly in the preribosome and can serve as a "distribution box," transmitting remodeling energy from Rea1 into the developing ribosome. We suggest that a relay-like factor network coupled to a mechano-enzyme is strategically positioned to relocate rRNA elements during ribosome maturation.

Introduction

Ribosomes, the cellular protein-synthesizing machines, are composed of four ribosomal RNAs (18S, 25S, 5.8S, and 5S rRNA) and ∼80 ribosomal proteins, organized into large (60S) and small (40S) subunits. Eukaryotic ribosome synthesis is a complicated process. It includes transcription, modification, processing, and folding of the rRNA, which is coordinated with the assembly of the ribosomal proteins (r-proteins). Ribosome formation is catalyzed by ∼200 biogenesis factors that participate in the successive assembly and maturation steps, eventually leading to mature ribosomal subunits (Fromont-Racine et al., 2003; Tschochner and Hurt, 2003; Henras et al., 2008; Woolford and Baserga, 2013). Among these are several energy-consuming enzymes including the Rea1 ATPase, which is structurally related to the motor protein dynein. Rea1 consists of a hexameric ATPase associated with diverse cellular activities (AAA) motor ring, and a long flexible tail. The Rea1 tail protrudes from the AAA motor ring and ends with a metal ion–dependent adhesion site (MIDAS). The MIDAS is a protein–protein interaction motif typically found in integrins, where it tethers extracellular ligands to the plasma membrane. Rea1 couples ATP hydrolysis to the generation of a mechano-chemical force that removes biogenesis factors from the maturing pre-60S particle. Rsa4 is a cofactor and direct substrate of Rea1, and both biogenesis factors are present on the Rix1 particle, a distinct pre-60S intermediate located in the nucleoplasm (Ulbrich et al., 2009; Baßler et al., 2010; Kressler et al., 2010, 2012b). Binding of the Rea1 MIDAS region to a conserved acidic residue (E114) in the Rsa4

*J. Baßler and H. Paternoga contributed equally to this paper.

**E. Barbar, I. Sinning, and E. Hurt contributed equally to this paper.

Correspondence to Ed Hurt: ed.hurt@bzh.uni-heidelberg.de; Irmi Sinning: irmi.sinning@bzh.uni-heidelberg.de; or Elisar Barbar: barbare@science.oregonstate.edu

Abbreviations used in this paper: AAA, ATPase associated with diverse cellular activities; CRAC, UV cross-linking and analysis of cDNA; ITC, isothermal titration calorimetry; MIDAS, metal ion–dependent adhesion site; NMR, nuclear magnetic resonance; PTC, peptidyl transferase center; rRNA, ribosomal RNA; SEC, size-exclusion chromatography; TEV, tobacco etch virus; UBL, ubiquitin-like.

The Rockefeller University Press $30.00
J. Cell Biol. Vol. 207 No. 4 481–498
www.jcb.org/cgi/doi/10.1083/jcb.201408111

Table 1. **Yeast strains used in this study**

Name	Genotype	Reference
DS1-2b	*his3-Δ200 leu2-Δ1, trp1-Δ63 ura3-52, MATα*	Nissan et al., 2002
Nsa2-FTpA	P_{NSA2} *NSA2-LINKER-FTpA::natNT2, ade2, his3, leu2, trp1, ura3, MATα* (linker: ASSYTAPQPGLGGS)	This study
W303a	*ade2-1, his3-11,15, leu2-3,112,trp1-1, ura3-1, can1-100, MATa*	Thomas and Rothstein, 1989
W303α	*ade2-1, his3-11,15, leu2-3,112,trp1-1, ura3-1, can1-100, MATα*	Thomas and Rothstein, 1989
Y3719 Rsa4Δ Nmd3Δ	*rsa4::HIS3MX4, nmd3::kanMX6, ade2-1, his3-11,15, leu2-3,112,trp1-1, ura3-1, can1-100, MATa*	This study
Y3978 Rsa4 shuffle	*rsa4::kanMX6, ade2-1, ura3-1,his3-11.15, leu2-3.112, trp1-1, can1-100, MATa,* pRS316-*RSA4*	Ulbrich et al., 2009
Y3983 Rsa4Δ, Rix1Δ	*rsa4::HIS3, rix1*::kanMX4, *his3, trp1, leu2, ura3, MATα* pRS316-*RSA4*, pRS316-*RIX1*	This study
Y3996 Rsa4Δ, Ipi3Δ	*rsa4::HIS3, ipi3*::kanMX4, *his3, trp1, leu2, ura3, MATα* pRS316-*RSA4*, pRS316-*IPI3*	This study
Y4073 PJ69-4a	*trp1-901, leu2-3,112, ura3-52, his3-200, gal4Δ, gal80Δ, LYS2::GAL1-HIS3, GAL2-ADE2, met2::GAL7-lacZ, MATa,*	James et al., 1996
Y4267 Nsa2 shuffle	*nsa2::kanMX6, ade2-1, ura3-1, his3-11.15, leu2-3.112, trp1-1, can1-100, MATa, pRS316-NSA2*	This study
Y4268 Nsa2 shuffle	*nsa2::kanMX6, ade2-1, ura3-1, his3-11.15, leu2-3.112, trp1-1, can1-100, MATα, pRS316-NSA2*	This study
Y4466 Rpl5 shuffle	*rpl5::HIS3MX4 (Rpl5 = uL18), ade3::kanMX4, ade2-1, his3-11,15, leu2-3,112,trp1-1, ura3-1, can1-100, MATα, pHT4467-RPL5*	This study
Y4586 Rsa4Δ, Nsa2Δ	*Nsa2::kanMX6,rsa4::kanMX6, ade2-, ura3-1, his3-11.15, leu2-3.112, trp1-1, can1-100,* MATa,pRS316-*NSA2*, pRS316-*RSA4*	This study
Y4591 Rsa4Δ Ytm1Δ	*rsa4::KanMX, ytm1::hphNT1, ade2-1, ura3-1, his3-11.15, leu2-3,112, trp1-1, MATα, pRS316-RSA4, pRS316-YTM1*	This study
Y4678 Rsa4Δ, Nog1Δ	*rsa4::kanMX6, nog1::kanMX6, his3, trp1, leu2, ura3, LYS2, ade2, MATα*, pRS316-*RSA4*, pURA3-*NOG1*	This study
Y4685 Rsa4Δ, Nug1Δ	*rsa4::HIS3, nug1*::kanMX6, ura3, his3, leu2, trp1, *MATa*, pRS316-*RSA4*, pRS316-*NUG1*	This study
Y4940 TAP-Rsa4	P_{RSA4}*-TAP-FLAG-RSA4::natNT2, (2protA-TEV-CBP-FLAG-Rsa4) ade2, his3, leu2, trp1, ura3, MATa*	This study
Y4992 Nsa2Δ, Nog1Δ	*nsa2::kanMX6, nog1::kanMX6, his3, trp1, leu2, ura3, ade2, MATa* pRS316-*NSA2*, pURA3-*NOG1*	This study
Y5056 Nsa2-HIS-TEV-ProtA	*NSA2-His-TEV-protA::HIS3, ade2-1, his3-11,15, leu2-3,112, trp1-1, ura3-1, can1-100, MATα*	This study
Y5549 Arx1-FTpA Nsa2Δ	*Arx1-FTpA::natNT2, nsa2::kanMX6, ade2-1, ura3-1, his3-11.15, leu2-3.112, trp1-1, can1-100, MATa*	This study
Y5550 Arx1-FTpA Rsa4Δ	*Arx1-FTpA::natNT2, rsa4::HIS3MX6, ade2-1, ura3-1, his3-11.15, leu2-3.112, trp1-1, can1-100, MATa*	This study

N-terminal domain allows the Rea1 power stroke to pull on Rsa4 and eventually remove it from the preribosome (Ulbrich et al., 2009; Matsuo et al., 2014). However, it remains unclear whether Rsa4 dislocation is actively coupled to structural maturation of the pre-60S particle.

In this study, we demonstrate that Rsa4 is part of an assembly factor network, including ribosomal proteins and rRNA, which can funnel the mechano-chemical energy of Rea1 into the preribosome for remodeling. Our findings are based on several crystal and nuclear magnetic resonance (NMR) structures of Rsa4, Nsa2, and the Rsa4–Nsa2 complex, which together with recent cryo-EM data reveal how the essential Rsa4–Nsa2 complex is embedded into the RNA/protein network of the late pre-60S ribosome at pseudo-atomic resolution. Altogether, our data suggest that Rsa4 and Nsa2 establish a physical link between the Rea1 ATPase and the premature rRNA helix 89, which requires relocation to reach its final position at the peptidyl transferase center (PTC).

Results

Rsa4 interacts directly with Nsa2

Initially, we searched for proteins and/or rRNA regions that contact Rsa4 on the pre-60S particle and could potentially transmit remodeling energy from Rea1 into the maturing 60S subunit. To this end, we performed genetic analyses with the *rsa4-1* mutant allele (Ulbrich et al., 2009) to identify functional partners. This screen revealed synthetic lethal interactions between *RSA4* and several components of the Rix1 particle, including *RIX1*, *IPI3*, *NUG1*, and *NSA2* (Baßler et al., 2001; Galani et al., 2004; Nissan et al., 2004; Bassler et al., 2006; Lebreton et al., 2006; Fig. S1 A; the yeast strains and plasmids used are listed in Tables 1 and 2, respectively). Subsequent yeast two-hybrid and biochemical assays showed that Rsa4 forms a robust and stoichiometric complex with the 60S assembly factor Nsa2 (Figs. 1 A and S1 B). Notably, the plant (*Solanum chacoense)* homologues of Rsa4 and Nsa2 also show a two-hybrid interaction (Chantha and Matton,

Table 2. **Plasmids used in this study**

Name	Genotype	Reference/source
pADH181 *pA-TEV-ctrsa4* Δ1–29	*2μ, LEU2, AmpR, P_{ADH1} pA-TEV-ctrsa4* 30–517aa, *Chaetomium thermophilum* Rsa4	This study
pASΔΔ *NSA2*	2μ, TRP1, P_{ADH1} Gal4-DNA BD-NSA2	This study
pASΔΔ *nsa2 C* (ΔN4)	See above, pASΔΔ Nsa2 141–261 aa	This study
pASΔΔ *nsa2 N* (ΔC4)	See above, pASΔΔ Nsa2 1–144 aa	This study
pASΔΔ *nsa2 ΔN1*	See above, pASΔΔ Nsa2 77–261 aa	This study
pASΔΔ *nsa2 ΔN2*	See above, pASΔΔ Nsa2 35–261 aa	This study
pEcOmeTyr/ectRNA$_{CUA}$	CEN, TRP1, expression of amber suppressor ectRNACUA and aminoacyl ectRNA-synthetase	Chin et al., 2003
pET Duet1 *rsa4* Δ136	AmpR, P_{T7} *rsa4 ΔN 136 aa*	This study
pET24d *HIS$_6$-TEV-ctnsa2* 1–84	KanR, P_{T7} *HIS$_6$-TEV-ctnsa2* 1–84 aa *Chaetomium thermophilum* Nsa2	This study
pET24d *HIS$_6$-TEV-ctnsa2* 168–261	KanR, P_{T7} *HIS$_6$-TEV-ctnsa2* 168–261 aa *Chaetomium thermophilum* Nsa2	This study
pET24d HIS$_6$-TEV-*RSA4*	*KanR, P_{T7} HIS6-TEV-RSA4*	This study
pET24d *HIS$_6$-TEV-RSA4*	KanR, P_{T7} *HIS$_6$-TEV-RSA4*	This study
pET24d *HIS$_6$-TEV-rsa4* b1*	KanR, P_{T7} *HIS$_6$-TEV-rsa4 T175R,T177R*	This study
pET24d *HIS$_6$-TEV-rsa4* b8*	KanR, P_{T7} *HIS$_6$-TEV-rsa4 K130E,R134E*	This study
pET24d *HIS$_6$-TEV-rsa4 Y448E*	KanR, P_{T7} *HIS$_6$-TEV-rsa4 Y448E*	This study
pETM43 *MBP*	KanR, empty vector, P_{T7}, MBP control	EMBL Core facility
pETM43 *MBP-PRE-NSA2*	KanR, P_{T7} MBP-PRE-NSA2	This study
pETMBPxray_V43	*KanR, P_{T7}, MBP* (optimized for carrier-driven crystallization: *D82A, K83A, K239A, E359A, K362A, D363A*)-linker (AAAA) NcoI	This study
pETMBPxray_V43 *MBP-nsa2* 81–101	See above, Nsa2 peptide: 81–101 aa	This study
pETMBPxray_V43 *MBP-nsa2* 84–96	See above, Nsa2 peptide: 84–96 aa	This study
pG4ADHAN *RSA4*	*CEN, LEU2, P_{ADH1} GAL4-AD-RSA4* 1–515 aa	This study
pGADT7 *rsa4* MIDO	*2μ, LEU2, P_{ADH1} GAL4-AD-rsa4* 1–154 aa	Ulbrich et al., 2009
pHAC111 *NOG1*	*LEU2, NOG1-HA3*	Honma et al., 2006
pHAC111 *nog1-11*	LEU2, *nog1-11*-HA3	Honma et al., 2006
pnatNT2 P_{RSA4} *NTAP-FLAG*	*CEN, AmpR, P_{TEF1} natNT2 T_{ADH1}, P_{RSA4} 2× pA-TEV-CBP-FLAG*, integration cassette	This study
pRS314 *NSA2*	*CEN, TRP1, AmpR, P_{NSA2} NSA2*	This study
pRS314 *nsa2*-1	*CEN, TRP1, AmpR, P_{NSA2} nsa2-1*, point mutation in STOP leads to elongation of Nsa2p by 17 aa: RAKKCSVFFFFYLDGSN*	This study
pRS314 *nsa2-3*	*CEN, TRP1, AmpR, P_{NSA2} nsa2 N203K*	This study
pRS314 *nsa2-9*	*CEN, TRP1, AmpR, P_{NSA2} nsa2 S177R,H186P*	This study
pRS314 *RSA4*	*CEN, TRP1, AmpR, P_{RSA4} RSA4*	Ulbrich et al., 2009
pRS314 *rsa4-1*	*CEN, TRP1, AmpR, P_{RSA4} rsa4-1*	Ulbrich et al., 2009
pRS315 *IPI3*	*CEN, LEU2, AmpR, P_{IPI3} IPI3*	This study
pRS315 *ipi3-2*	*CEN, LEU2, AmpR, P_{IPI3} ipi3-2*	This study
pRS315 *NSA2*	*CEN, LEU2, AmpR, P_{NSA2} NSA2*	This study
pRS315 *nsa2 Y90A*	*CEN, LEU2, AmpR, P_{NSA2} nsa2 Y90A*	This study
pRS315 *nsa2 Y90F*	*CEN, LEU2, AmpR, P_{NSA2} nsa2 Y90F*	This study
pRS315 *rix1-1*	CEN, LEU2, AmpR, P_{RIX1} *rix1-1*	Baßler et al., 2001
pRS315 *RSA4*	*CEN, LEU2, AmpR, P_{RSA4} RSA4*	Ulbrich et al., 2009
pRS315 *rsa4-1*	*CEN, LEU2, AmpR, P_{RSA4} rsa4-1*	Ulbrich et al., 2009
pRSF Duet1 *GST-TEV-NSA2 + HIS$_6$-TEV-RSA4*	*KanR, P_{T7} GST-TEV-NSA2 + P_{T7} HIS$_6$-TEV-RSA4*	This study
pRSF Duet1 *GST-TEV-NSA2* Δ85–98 + *HIS$_6$-TEV-RSA4*	*KanR, P_{T7} GST-TEV-nsa2* Δ 85–98 aa + *P_{T7} HIS$_6$-TEV-RSA4*	This study
pRSF Duet1 *GST-TEV-NSA2* Δ86–90 + *HIS$_6$-TEV-RSA4*	*KanR, P_{T7} GST-TEV-nsa2* Δ 86–90 aa + *P_{T7} HIS$_6$-TEV-RSA4*	This study
pT7 HIS$_6$-*rsa4 ΔN*	*KanR, P_{T7} HIS6-RSA4 ΔN* 112–516 aa	This study
pT7 *HIS$_6$-TEV-rsa4* ΔN26	KanR, P_{T7} *HIS$_6$-TEV-rsa4* 27–515 aa	This study
pTD1-1	*2μ, LEU2, GAL4 AD-SV40 large T-antigen* (84-708 aa), pACT2	Takara Bio Inc.
pUN100 *RIX1*	CEN, LEU2, AmpR, P_{RIX1} RIX1	Baßler et al., 2001
pVA3-1	*2μ, TRP1, GAL4 DNA BD-murine p53* (72–390 aa), pGBT9	Takara Bio Inc.
YCplac111 *NSA2-FTpA*	*CEN, LEU2, AmpR, P_{NSA2} NSA2-LINKER-FLAG-TEV-pA*, Linker:ASSYTAPQPGLGGS	This study
YCplac111 *nsa2-FTpA* Δ85–98	See above, *P_{NSA2} nsa2-L-FTpA*, Δ 85–98 aa	This study
YCplac111 *nsa2-FTpA* Δ86–90	See above, *P_{NSA2} nsa2-L-FTpA*, Δ 86–90 aa	This study
YCplac111 *P_{GAL} NSA2-FTpA*	CEN, LEU2, AmpR, $P_{GAL1\text{-}10}$ NSA2-LINKER-FLAG-TEV–pA,Linker:ASSYTAPQPGLGGS	This study
YCplac111 *P_{GAL} nsa2-FTpA* Δ85–98	See above, *$P_{GAL1\text{-}10}$ nsa2-L-FTpA*, Δ 85–98 aa	This study

Table 2. **Plasmids used in this study** *(Continued)*

Name	Genotype	Reference/source
YCplac111 P_{GAL} *nsa2-FTpA* Δ86–90	See above, $P_{GAL1\text{-}10}$ *nsa2-L*-FTpA, Δ 86–90 aa	This study
YCplac111 *RPL5*	CEN, LEU2, *AmpR*, P_{Rpl5} *RPL5*	This study
YCplac111 *rpl5* Δloop2	See above, Δ 122–138 aa	This study
YCplac111 *rpl5* Δloop2+3	See above, Δ 122–138 aa, Δ185–198>R aa	This study
YCplac111 *rpl5* Δloop3	See above, Δ 185–198>R aa	This study
YCplac111 *RPL5*-FTpA	CEN,LEU2,*AmpR*,P_{RPL5} *RPL5-5xGA-FTpA*	This study
YCplac111 *rpl5*-FTpA Δloop2	See above, Δ 122–138 aa	This study
YCplac111 *rpl5*-FTpA Δloop2+3	See above, Δ 122–138 aa, Δ 185–198>R aa	This study
YCplac111 *rpl5*-FTpA Δloop3	See above, Δ 185–198>R aa	This study
YCplac111 *RPL5-GFP*	CEN, LEU2, *AmpR*, P_{RPL5} *RPL5-GFP*	This study
YCplac111 *rpl5-GFP* Δloop2+3	See above, Δ 122–138 aa, Δ 185–198>R aa	This study
YCplac111 *TAP-FLAG-rsa4* b1*	CEN, LEU2, *AmpR*, P_{RSA4} *pA-CBP-2×FLAG-rsa4 K130E,R134E*	This study
YCplac111 *TAP-FLAG-rsa4* b8*	CEN, LEU2, *AmpR*, P_{RSA4} *pA-CBP-2×FLAG-rsa4 T175R,T177R*	This study
YCplac111 *TAP-FLAG-rsa4 Y448E*	CEN, LEU2, *AmpR*, P_{RSA4} *pA-CBP-2×FLAG-rsa4 Y448E*	This study
YCplac22 *NSA2-FTpA*	*CEN, TRP1, AmpR*, P_{NSA2} *NSA2-LINKER-FLAG-TEV-pA*, Linker:ASSYTAPQPGLGGS	This study
YCplac22 *nsa2-FTpA Y90A*	*See above*, P_{NSA2} *nsa2-LINKER-FLAG-TEV-pA, nsa2 Y90A*, Linker:ASSYTAPQPGLGGS	This study
YEplac112 $P_{GAL1\text{-}10}$ *NSA2*	*2μ, TRP1, AmpR*, $P_{GAL1\text{-}10}$ *NSA2*	This study
YEplac112 $P_{GAL1\text{-}10}$ *nsa2 Y90A*	See above, $P_{GAL1\text{-}10}$ *nsa2 Y90A*	This study
YEplac112 $P_{GAL1\text{-}10}$ *RSA4*	See above, $P_{GAL1\text{-}10}$ *RSA4*	This study
YEplac112 $P_{GAL1\text{-}10}$ *rsa4* b1*	See above, $P_{GAL1\text{-}10}$ *rsa4 K130E,R134E*	This study
YEplac112 $P_{GAL1\text{-}10}$ *rsa4* b8*	See above, $P_{GAL1\text{-}10}$ *rsa4 T175R,T177R*	This study
YEplac112 $P_{GAL1\text{-}10}$ *rsa4 Y448E*	See above, $P_{GAL1\text{-}10}$ *rsa4 Y448E*	This study
YEplac181 $P_{GAL1\text{-}10}$ *NSA2* $P_{GAL1\text{-}10}$-tc-apt-2×HA-TAG-*RPL25*-FTpA	*2μ, LEU2, AmpR*, $P_{GAL1\text{-}10}$ *NSA2* T_{ADH1}, $P_{GAL1\text{-}10}$ tetracycline-aptamer-2×HA-amber-*RPL25*-FLAG-TEV-pA T_{ADH1}	This study
YEplac181 $P_{GAL1\text{-}10}$ *nsa2 Y90A* $P_{GAL1\text{-}10}$-tc-apt-2×HA-TAG-*RPL25*-FTpA	*2μ, LEU2, AmpR*, $P_{GAL1\text{-}10}$ *nsa2 Y90A* T_{ADH1} $P_{GAL1\text{-}10}$ tetracycline-aptamer-2×HA-amber-*RPL25*-FLAG-TEV-pA T_{ADH1}	This study

2007). Further deletion analyses revealed that a short linear motif in Nsa2, composed of residues 85–98, is required and sufficient to bind the WD40 β-propeller of Rsa4 (Fig. 1, A and B). Expression of Nsa2Δ85–98 in yeast failed to support growth of the lethal *nsa2Δ* mutant (Fig. 1 C) and caused a dominant-negative phenotype upon overexpression (Fig. 1 D). To analyze the affinity of the Rsa4–Nsa2 interaction, isothermal titration calorimetry (ITC) was performed between the β-propeller of Rsa4 and the Nsa2 peptide (85–95 aa), which revealed a K_d in the lower nanomolar range (Fig. 1 E). We conclude that a short sequence in Nsa2 is required to generate a robust contact to Rsa4.

Structural basis of the Rsa4–Nsa2 interaction

To gain structural insights into the Rsa4–Nsa2 interaction, we first determined the crystal structures of Rsa4 from *Chaetomium thermophilum* (*ct*Rsa4ΔN30) and *Saccharomyces cerevisiae* (*sc*Rsa4ΔN26) at 1.8 Å and 2.9 Å resolution, respectively (Figs. 2 A and S2 A; statistics of crystal structures are listed in Table 3). Rsa4 consists of an N-terminal ubiquitin-like (UBL) domain and a C-terminal eight-bladed β-propeller domain. Blade 5 of the propeller harbors a long loop insertion (residues 330–371 of *ct*Rsa4) with a prominent α-helix (shown in purple in Fig. 2 A) that is docked onto the bottom side of the β-propeller. A short loop protruding from the UBL domain harbors the highly conserved glutamic acid E117 (E114 in yeast; indicated in purple in Fig. 2 A), which is exposed on the surface. Interaction of this residue with the Rea1 MIDAS domain is essential for ATP-dependent removal of Rsa4 from the pre-60S particle (Ulbrich et al., 2009), probably by contributing to the coordination of the Rea1 MIDAS-associated cation. The *sc*Rsa4 crystal contains two molecules in the asymmetric unit, which differ in the relative orientation of the UBL to the β-propeller (Fig. S2 A). This rotational flexibility could be of functional importance in dynamically transmitting the power stroke of Rea1 into the maturing pre-60S particle.

Although our attempts to crystallize Nsa2 failed, probably because of flexible regions in the protein, we were able to determine NMR solution structures of two major domains (statistics of NMR structures are listed in Table 4). The *ct*Nsa2 C-terminal region (residues 168–261) adopts a six-stranded β-barrel fold (Fig. 3 A), which is closely related to the β-barrel fold of ribosomal protein Rps8 (eS8) that directly binds rRNA (Fig. 3, A and B; Ben-Shem et al., 2011; Rabl et al., 2011). Several different solution structures were identified for the Nsa2 N domain (residues 1–84), which all reveal two prominent α-helices connected by a flexible linker sequence (Fig. 3 C). The first helix is rigid, with a kink at the N terminus, whereas the second helix shows variability in its orientation and length. The Nsa2 conformation may be stabilized upon binding to the preribosome (see the last paragraph of the Results section).

To characterize the interaction between Rsa4 and Nsa2, the Rsa4-interacting peptide of Nsa2 (residues 81–101) was fused to a carrier protein (MBP) and cocrystallized with the Rsa4 β-propeller domain (Figs. 2 B and S2 B). The structure of this minimal heterodimer was solved at 3.2 Å resolution and

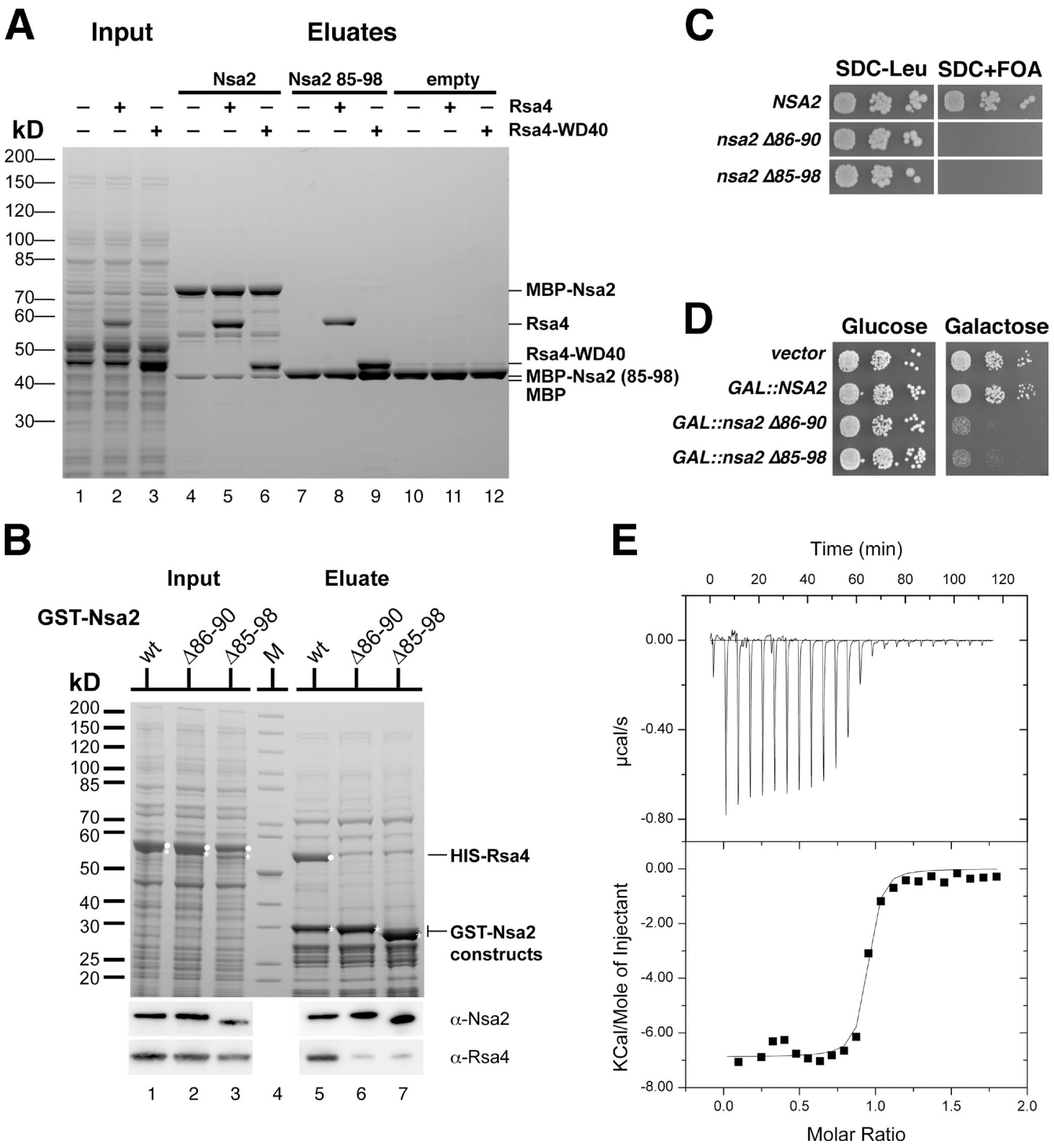

Figure 1. **A short peptide within Nsa2 is essential for binding to Rsa4.** (A) In vitro binding assay of MBP-Nsa2 with Rsa4. Purified MBP-Nsa2 (lane 4–6), MBP-Nsa2 84–96 aa (lane 7–9), and MBP (lane 10–12) were immobilized on amylose beads and incubated with *E. coli* lysate without or with HIS_6-TEV-Rsa4 full-length or HIS_6-Rsa4 WD40 domain, respectively (lane 1–3). Eluates were analyzed by 4–12% SDS-PAGE and stained with Coomassie blue. (B) In vitro copurification of GST-Nsa2 and Rsa4. GST-Nsa2 wild-type, GST-Nsa2Δ86–90, or GST-Nsa2Δ85–98 were coexpressed with HIS-Rsa4 (input; see lanes 1, 2, and 3), purified via GSH Sepharose, and eluted by TEV cleavage (lanes 5, 6, and 7). The 4–12% SDS-polyacrylamide gel was stained with Coomassie blue, and Rsa4 and Nsa2 were detected by Western blot analysis. (C) Viability of *nsa2* deletion mutants. An Nsa2 shuffle strain was transformed with plasmids encoding the indicated *NSA2* alleles tagged with FTpA. Transformants were analyzed for complementation by spotting a 1:10 dilution series on SDC+FOA. The growth phenotype after 3 d of incubation at 30°C is shown. (D) Dominant-negative phenotype of *nsa2* deletion mutants. Wild-type strain W303 was transformed with plasmids expressing the indicated *NSA2* alleles tagged with FTpA under the control of the inducible *GAL10* promoter. The toxic effect of *NSA2* overexpression was tested on galactose-containing medium (SGC-TRP) after incubation for 3 d at 30°C. (E) ITC measurement of Rsa4 β-propeller with Nsa2 peptide is shown. Recombinant Rsa4 β-propeller (Rsa4Δ136) was expressed in *E. coli*, affinity-purified, and further purified by SEC before ITC measurement was performed with synthesized Nsa2 peptide (85–95 aa, DALPTYLLDRE).

Table 3. **Data collection and refinement statistics of crystal structures**

Criteria	*ct*Rsa4	*sc*Rsa4	*sc*Rsa4 + *sc*Nsa2 peptide
Data collection			
Space group	P1	I 222	C2
Cell dimensions			
α, β, χ (Å)	48.15, 48.83, 58.63	96.87, 108.47, 261.91	198.58, 96.49, 196,45
α, β, γ (°)	67.47, 88.39, 62.65	90, 90, 90	90, 115.45, 90
Resolution (Å)	42.07–1.80 (1.90–1.80)[a]	43.61–2.80 (2.90–2.80)[a]	48.98–3.20 (3.30–3.20)[a]
R_{merge}	0.044 (0.284)	0.094 (0.472)	0.168 (0.875)
$I/\sigma I$	6.7 (2.5)	7.7 (2.2)	15.6 (3.1)
Completeness (%)	94.7 (93.3)	97.3 (98.6)	100 (100)
Redundancy	1.8 (1.8)	1.9 (1.9)	11.4 (11.5)
Refinement			
Resolution (Å)	43.02–1.80	43.61–2.80	48.98–3.20
No. reflections	37783	33498	55659
R_{work}/R_{free}	0.1678/0.2127	0.2017/0.2549	0.2184/0.2571
No. atoms			
Protein	3848	7219	23533
Water	432		142
B-factors		47.10	
Protein	32.80		27.80
Water	39.10	0.010	17.80
Rms deviations		1.397	
Bond lengths (Å)	0.004		0.002
Bond angles (°)	0.87		0.64
Validation			
Ramachandran plot (%)			
Favored	96.5	90.5	96.2
Allowed	3.5	7.5	3.7
Outliers	0.0	2	0.1
MolProbity clash score	4.20	8.55	5.46

One crystal was used for structure solution.
[a]Highest resolution shell is shown in parenthesis.

reveals how the Nsa2 peptide contacts the top side of the eight-bladed Rsa4 β-propeller, opposite to the Rsa4 UBL domain with its Rea1 MIDAS binding loop. Nsa2 residues 85–95 form a short helical segment that is deeply inserted into a cavity of the β-propeller, with ∼1,300 Å^2 of buried surface area. This cavity is characterized by a hydrophobic ring formed by tryptophan and tyrosine residues (Fig. 2 B). The interaction is predominantly hydrophobic, but salt bridges ($R94_{Nsa2}$–$E379_{Rsa4}$; $E93_{Nsa2}$–$K256_{Rsa4}$) and hydrogen bonds ($Y90_{Nsa2}$–$Y490_{Rsa4}$) also contribute to the interface.

The interaction between Rsa4 and Nsa2 is essential for 60S biogenesis

To assess the functional relevance of the Rsa4–Nsa2 interaction, structure-based mutations in the Nsa2 binding peptide were generated to impair the binding to Rsa4. Mutation of the highly conserved tyrosine 90 to alanine (*nsa2 Y90A*; Fig. S3 D) blocked complex formation with Rsa4 in vitro, whereas the more conservative mutation to phenylalanine (Y90F) still allowed binding (Fig. 4 A). Consistent with these findings, cells expressing *nsa2 Y90F* exhibited normal growth, whereas *nsa2 Y90A* cells were nonviable (Fig. 4 B). However, the mutant Nsa2 Y90A protein was still associated with pre-60S particles (Figs. 4 E and S3 A), which appeared to be independent of its interaction with Rsa4. Consistent with this interpretation, overexpression of Nsa2 Y90A protein caused a strong dominant-lethal phenotype, with replacement of endogenous Nsa2 within the preribosomes and a concomitant specific block in nuclear export and formation of 60S subunits (Fig. 4, C and F; and Fig. S3, A and C). To identify the step in ribosome biogenesis that is blocked by induction of *GAL::nsa2 Y90A*, we used a nonradioactive pulse-chase method combined with isolation of ribosomes via ribosomal protein Rpl25 (uL23; Stelter and Hurt, 2014). This confirmed that induction of *GAL::nsa2 Y90A* blocked production of mature 60S subunits, and caused the accumulation of pre-60S particles containing Nsa2 Y90A and Rsa4, in addition to a distinct set of pre60S factors, including Nog1, Nug1, Nog2, Arx1, Nsa3, Rpf2, and Rlp7 (Fig. 4 D). Strikingly, two methyl-transferases, Spb1 and Nop2, were strongly enriched in this arrested preribosomal intermediate. Both act on the PTC, with Nop2 modifying C2870 in helix H89 and Spb1 modifying G2922 in H92 (Lapeyre and Purushothaman, 2004; Sharma et al., 2013). This suggests that the Nsa2–Rsa4 interaction might be required for a distinct step in the structural maturation of the PTC during 60S subunit biogenesis.

Additional structure-based mutations were designed in the rim of the Rsa4 β-propeller that accommodates the Nsa2 peptide. Here, the Rsa4 Y448E mutation impaired binding to Nsa2

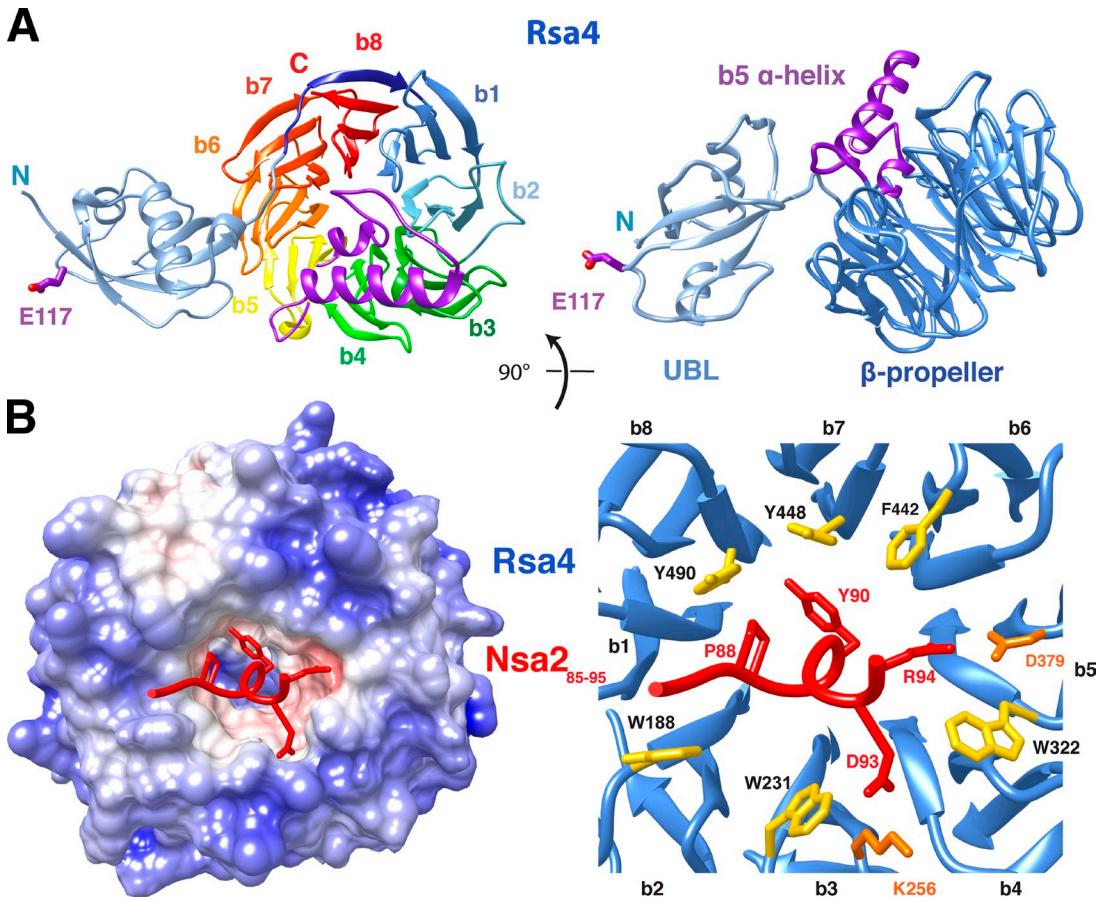

Figure 2. **Structural insight into the Rsa4–Nsa2 interaction.** (A) Crystal structure of *ct*Rsa4. Rsa4 consists of a UBL-like domain (light blue) followed by an eight-bladed β-propeller (left, b1–b8 in rainbow colors from dark blue to red; right, β-propeller rotated by 90° in dark blue) harboring the indicated α-helical insertion (purple) within blade 5. The highly conserved E117 (E114 in yeast) is also depicted, exposed on the surface of the UBL domain. (B) Crystal structure of the minimal *sc*Rsa4–*sc*Nsa2 complex. The surface view of *sc*Rsa4 is colored according to the charge calculated by PDB2PQR and APBS implemented in UCSF Chimera (left) with *sc*Nsa2 peptide (residues 86–95, red) bound into a hydrophobic pocket at the top site of the *sc*Rsa4 β-propeller (left). Also shown is a ribbon representation of the Nsa2 peptide (red) with its protruding residues bound to the *sc*Rsa4 β-propeller (blue) with hydrophobic (yellow) and charged residues involved in polar interactions (orange) at the rim of the propeller (right).

in vitro (Fig. S4 A) and blocked cell growth in vivo (Fig. S4 B). However, *GAL*-induced overexpression of the Rsa4 Y448E mutant protein caused a less pronounced dominant-negative phenotype (Fig. S4, C and E). This may be linked to the observation that Rsa4 Y448E is partly impaired in association with pre-60S particles (Fig. S4 D). Collectively, these experiments demonstrate the importance of the Rsa4–Nsa2 interaction for 60S maturation.

Rsa4 is located in close proximity to the premature central protuberance

We hypothesized that the mechano-chemical force generated by the Rea1 ATPase could be transmitted into the preribosome through the Rsa4–Nsa2 linkage. To test this model, we determined the precise positions of Rsa4 and Nsa2 within the nascent ribosome. We previously reported the cryo-EM structure of the Arx1-associated pre-60S particle, which contains a twisted 5S RNP (Bradatsch et al., 2012; Leidig et al., 2014). This particle also carries Rsa4 and Nsa2, but the location of Nsa2 in this assembly intermediate could not be determined, and our initial fit of Rsa4 was based on a molecular model using a nonrelated β-propeller and UBL domains as templates, which revealed only an approximate location between the 5S RNP and the stalk base (Leidig et al., 2014). Importantly, our new high-resolution Rsa4 crystal structure allowed us to precisely fit Rsa4 into the pre-60S cryo-EM map at pseudo-atomic resolution. The key for this improved fit was the bulging α-helical insertion in the Rsa4 β-propeller domain (Fig. 5 A), which served as an unambiguous landmark. Accordingly, β-propeller blades 3 and 4 of Rsa4 contact the undeveloped Rpl12-Rpp0 (uL11-uL10) stalk (which carries Mrt4 as a placeholder for r-protein Rpp0), blades 6 and 7 bind to a structure close to the PTC, and blades 1 and 8 interact with the nascent central protuberance (CP), which is composed of Rpl5 (uL18)–Rpl11 (uL5)–5S RNA (Fig. 5 B; Leidig et al., 2014).

Closer inspection revealed that Rsa4 blades 1 and 8 form an extended contact zone with the universally conserved Rpl5 protein, which faces the interface side of the nascent 60S subunit due to the relocated 5S RNP (Fig. 5 B; Leidig et al., 2014). Remarkably, this connection predominantly involves two eukaryote-specific loop insertions of Rpl5 (loop2 residues 122–138; loop3 residues 185–198; Fig. 5 B and Fig. 6, A and E). Deletion of the two eukaryotic-specific loops of Rpl5 (Rpl5Δloop2+3) resulted in a lethal phenotype (Fig. 6 D). Moreover, the Rpl5Δloop2+3

Table 4. **Statistics of NMR structures**

Criteria	*ct*Nsa2-C	*ct*Nsa2-N
NOE-derived distance constraints		
Sequential [(i − j) = 1]	766	
Medium Range [1 < (i − j) ≤ 5]	176	
Long Range [(i − j) > 5]	400	
Total	1,342	
Dihedral angle constraints		
φ	53	
ψ	56	
H-bonding constraints	28	
Number of constraints per residue	15.7	
Number of long-range constraints per residue	4.3	
Average RMSD to the mean CYANA coordinates [Å]		
All heavy atoms	1.3	
Backbone heavy atom (178-204, 215-224, 235-261)	0.80	
PROCHECK Z-scores (φ and ψ/all dihedral angles)	−1.41/−1.42	
MOLPROBITY mean score/clash score	11.08/2.20	
Ramachandran plot summary for ordered residues [%]		
Most favored regions	98.7	
Additionally allowed regions	1.3	
Disallowed regions	0.0	
Restraint violations		
CYANA target function [Å]	0.27	
Average number of distance violations per CYANA conformer [Å] > 0.5	0	
Average number of dihedral-angle violations per CYANA conformer [degrees]	0	
Average number of Van der Waal violations per CYANA conformer [Å] > 0.5	0	
CS-Rosetta input		
$^{13}C^{\alpha}$ shifts		77
$^{13}C^{\beta}$ shifts		73
$^{13}C'$ shifts		68
^{15}N shifts		69
$^{1}H^{N}$ shifts		69
$^{1}H^{\alpha}$ shifts		45

mutant accumulated inside the nucleus (Fig. 6 C), indicating that the loss of interaction with Rsa4 induces a defect during ribosome assembly. Affinity-purified Rpl5Δloop2+3 recovered its import factor Syo1 (Kressler et al., 2012a) and pre-60S particles. These included normal amounts of Nsa2, but had reduced levels of Rsa4 and lacked Rpl10 (uL16), a ribosomal protein assembling late into the maturing 60S subunit (Fig. 6 B). Additionally, methyl-transferases Spb1 and Nop2 were enriched in preribosomes associated with Rpl5Δloop2+3. In contrast, wild-type Rpl5, affinity-purified under similar conditions, only recovered mature 60S subunits, plus Syo1.

Likewise, structure-based mutations in Rsa4 blade 1 (*rsa4* b1*, *T175R*, *T177R*) and blade 8 (*rsa4* b8*, *K130E*, *R134E*) that contact the Rpl5 loops failed to support growth of the *rsa4Δ* strain (Fig. S4 B). These mutant Rsa4 proteins were still recruited to pre-60S particles, and, accordingly, their overexpression impaired subsequent biogenesis steps (Fig. S4, C–E). Thus, the contact between Rsa4 and Rpl5 is required for a preribosomal maturation step that is linked to the same methyl-transferases like the *nsa2 Y90A* mutant (Fig. 4 D), which have been shown to directly act on the nascent PTC (Lapeyre and Purushothaman, 2004; Sharma et al., 2013).

Nsa2 contacts rRNA helix 89 prior to its relocation to the PTC

After fitting the crystal structures of Rsa4 and the Nsa2 peptide into the high-resolution pre-60S cryo-EM map at 8.7 Å resolution (Fig. 5), we noticed an additional density that is visible on top of the Rsa4 β-propeller (Fig. 5 A, right). This density is located at the position where the Nsa2 peptide (residues 80–98) is docked to Rsa4 (Figs. 1 A and 2 B). Because the density closely resembles the shape and orientation of the Nsa2 peptide, as it is bound to Rsa4 in the crystal structure, we propose that it represents Nsa2, which is positioned in the same way in the pre-60S subunit. Notably, one end of the Nsa2 peptide projects toward rRNA helix 89 (Fig. 7, B and D), which forms part of the PTC, but is not yet repositioned to its mature location in this pre-60S particle (see Leidig et al., 2014; Video 1). To determine whether Nsa2 binds to the rRNA in this area of the preribosome, we applied the UV cross-linking and analysis of cDNA (CRAC) technique (Granneman et al., 2009, 2010). Nsa2-His_6-TEV-ProtA was UV cross-linked in vivo to H89 (60% of hits), H90 (25%), and H42 (15%; Figs. 7 A and S5). In the recovered cDNA sequences, specific point mutations suggest that there are direct Nsa2-binding sites on the rRNA (Fig. S5 B). The location of the

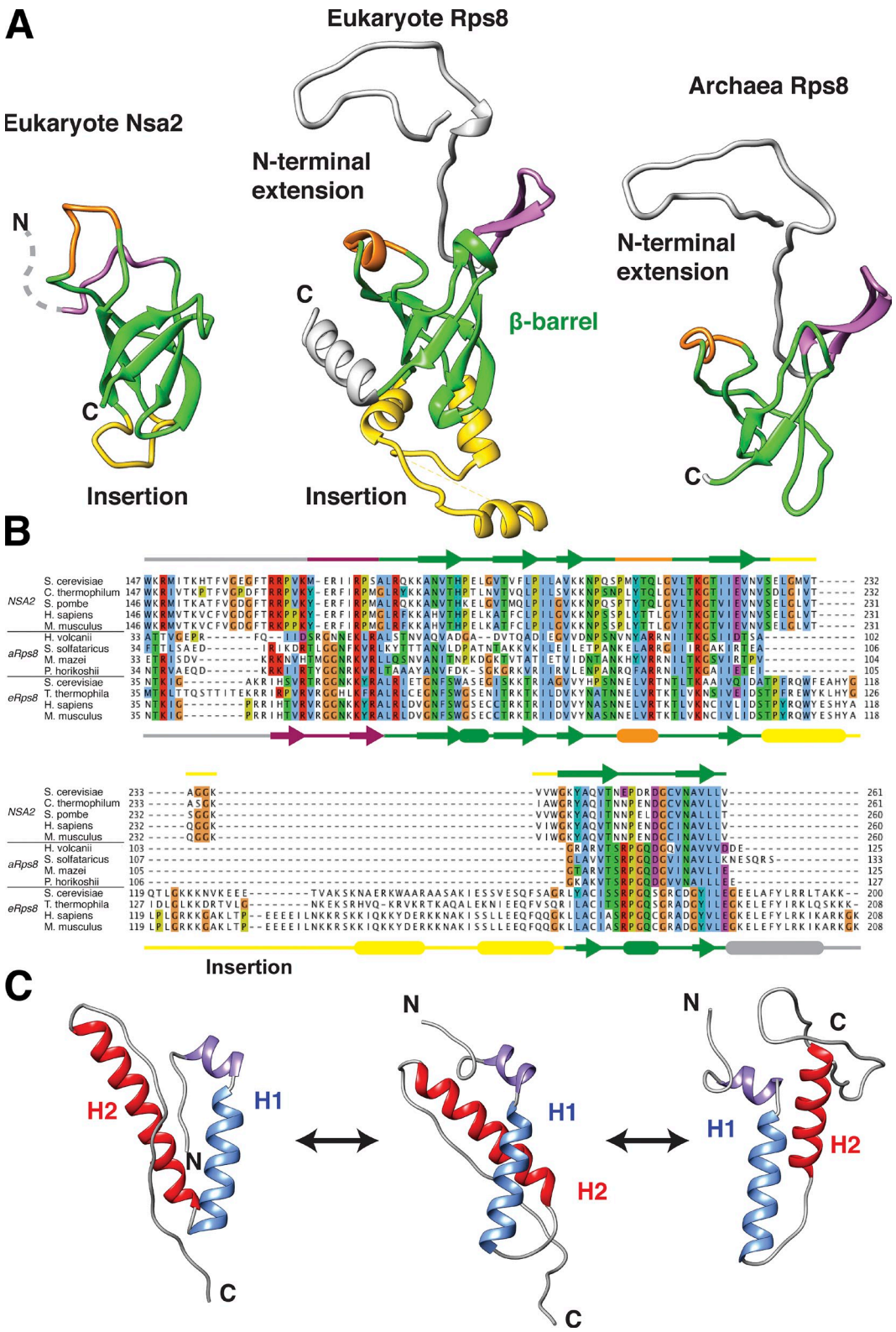

Figure 3. **NMR solution structures of *ct*Nsa2 domains.** (A) NMR structure of recombinant *ct*Nsa2-C (168–261 aa) adopts an Rps8 (eS8)-like six-stranded β-barrel fold. A structural similarity search of the protein databank performed with the DALI server identified the 40S ribosomal protein Rps8 (PDB accession no. 3U5C, chain I) from *S. cerevisiae* (S288c; sequence identity of 22%, Z score = 5.3, RMSD 3.7 Å) as structurally similar to *ct*Nsa2 168–261 aa. The right panel shows the structure of an archaeal Rps8 taken from the PDB (accession no. 3J43). The six-stranded β-barrel fold is shown in green; variable insertions are shown in yellow, orange, and purple. (B) Multiple sequence alignment including Nsa2, archaeal Rps8 (aRps8), and eukaryotic Rps8 (eRps8). Secondary structure elements are indicated for ctNsa2 on top (derived by NMR) and *S. cerevisiae* Rps8 (PDB accession no. 3U5C) below. (C) Representative NMR structures of *ct*Nsa2-N, determined by CS-Rosetta, show a common fold composed of one short N-terminal α-helix followed by two longer α-helices (H1 and H2). Multiple structures that differ in the packing and orientation of helix 2 reflect the disorder in the linker connecting the helices and the dynamic nature of Nsa2-N in solution.

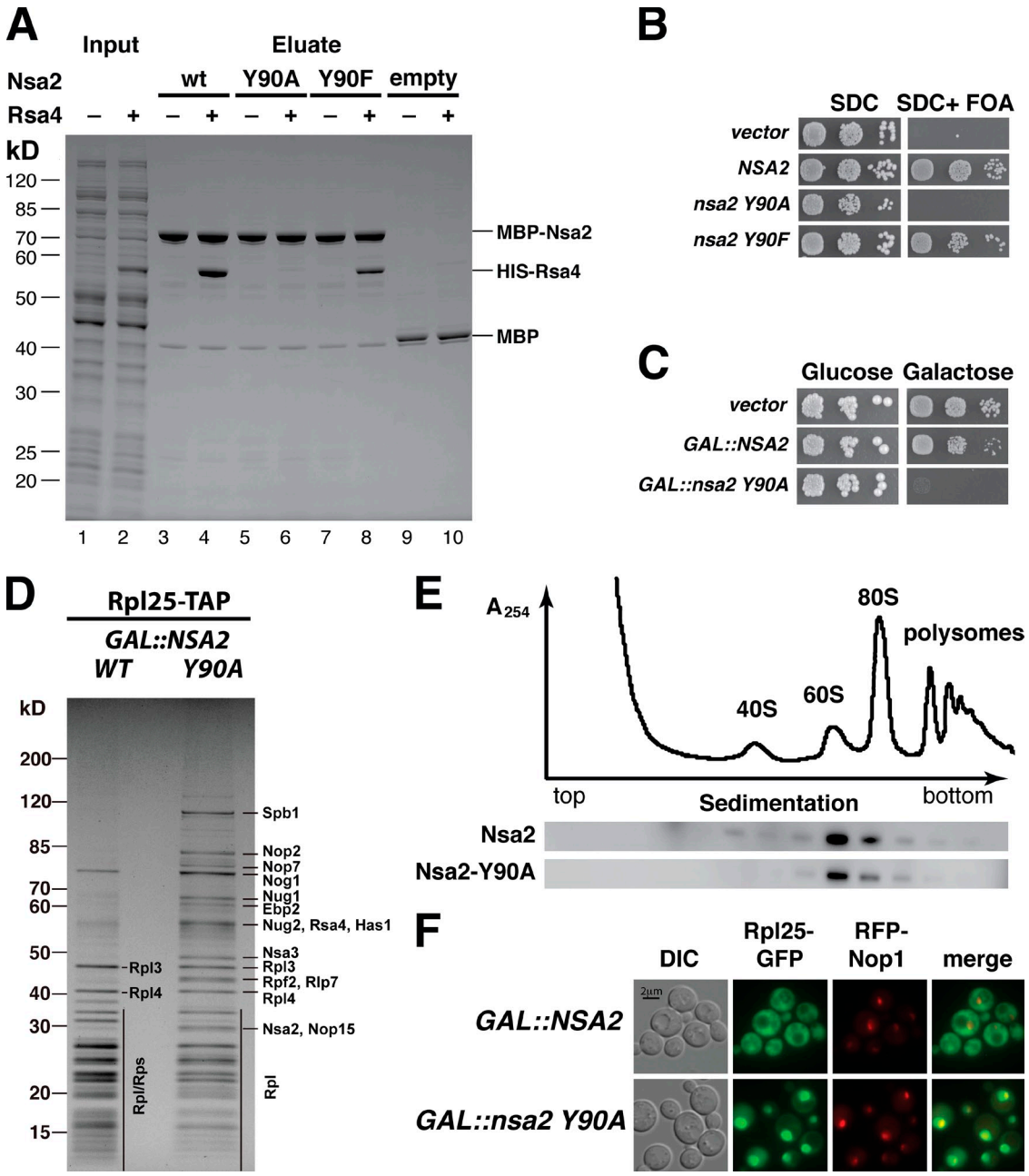

Figure 4. **The Rsa4–Nsa2 interaction is essential for ribosome biogenesis.** (A) In vitro reconstitution of the Nsa2–Rsa4 interaction. Purified MBP-Nsa2 wild-type (wt; lanes 3 and 4), Nsa2 Y90A (lanes 5 and 6), Nsa2 Y90F (lanes 7 and 8), and MBP alone (lanes 9 and 10) were immobilized on amylose beads and incubated with *E. coli* lysate with or without HIS-TEV-Rsa4 (for input, see lanes 1 and 2). Eluates were analyzed by 4–12% SDS-PAGE and Coomassie staining, and the positions of the bands are indicated. (B) The highly conserved tyrosine 90 in Nsa2 is essential for yeast cell growth. Nsa2 shuffle strain was transformed with plasmids carrying the *NSA2* or the indicated *nsa2* mutant alleles. Complementation was analyzed by incubation of transformants on SDC+FOA plates at 30°C for 2 d. (C) Overexpression of *nsa2 Y90A* is dominant lethal. A yeast wild-type strain with endogenous *NSA2* was transformed with 2μ plasmids carrying *NSA2* or *nsa2 Y90A* alleles under the control of the galactose-inducible *GAL* promoter. The dominant-negative phenotype by *NSA2* overexpression was tested on galactose-containing plates after incubation for 3 d at 30°C. (D) Dominant-lethal *nsa2 Y90A* induction arrests 60S biogenesis. Pulse-chase analysis of HA-Rpl25-Flag-ProtA (uL23) isolated from cells expressing dominant-negative *nsa2 Y90A* and wild-type *Nsa2*. HA-Rpl25-Flag-ProtA was pulsed for 7 min with Ome-Tyr after a 60-min galactose induction, and subsequently chased for 20 min with glucose/tetracycline in cells expressing *GAL::NSA2* (WT) or *GAL::nsa2 Y90A* (Y90A). Affinity-purified HA-Rpl25-Flag-ProtA was analyzed by SDS-PAGE and Coomassie staining, and bands were identified by mass spectrometry. (E) Mutant Nsa2 Y90A is efficiently assembled into preribosomes. Whole-cell lysates derived from wild-type cells expressing plasmid-borne *NSA2-FTpA* and *nsa2 Y90A-FTpA*, respectively, were fractionated on a 10–50% sucrose gradient, and fractions were analyzed by Western blotting using anti-ProtA antibodies to detect wild-type and mutant Nsa2 proteins. (F) Dominant-lethal *nsa2 Y90A* induction causes a defect in 60S subunit export. Wild-type yeast cells were transformed with plasmids harboring the 60S reporter Rpl25-EGFP (uL23) and mRFP-Nop1, and 2μ plasmids harboring *GAL::NSA2* or *GAL::nsa2 Y90A* alleles, respectively. Cells were shifted to galactose-containing medium for 6 h before intracellular localization of Rpl25-EGFP, and mRFP-Nop1 was analyzed by fluorescence microscopy.

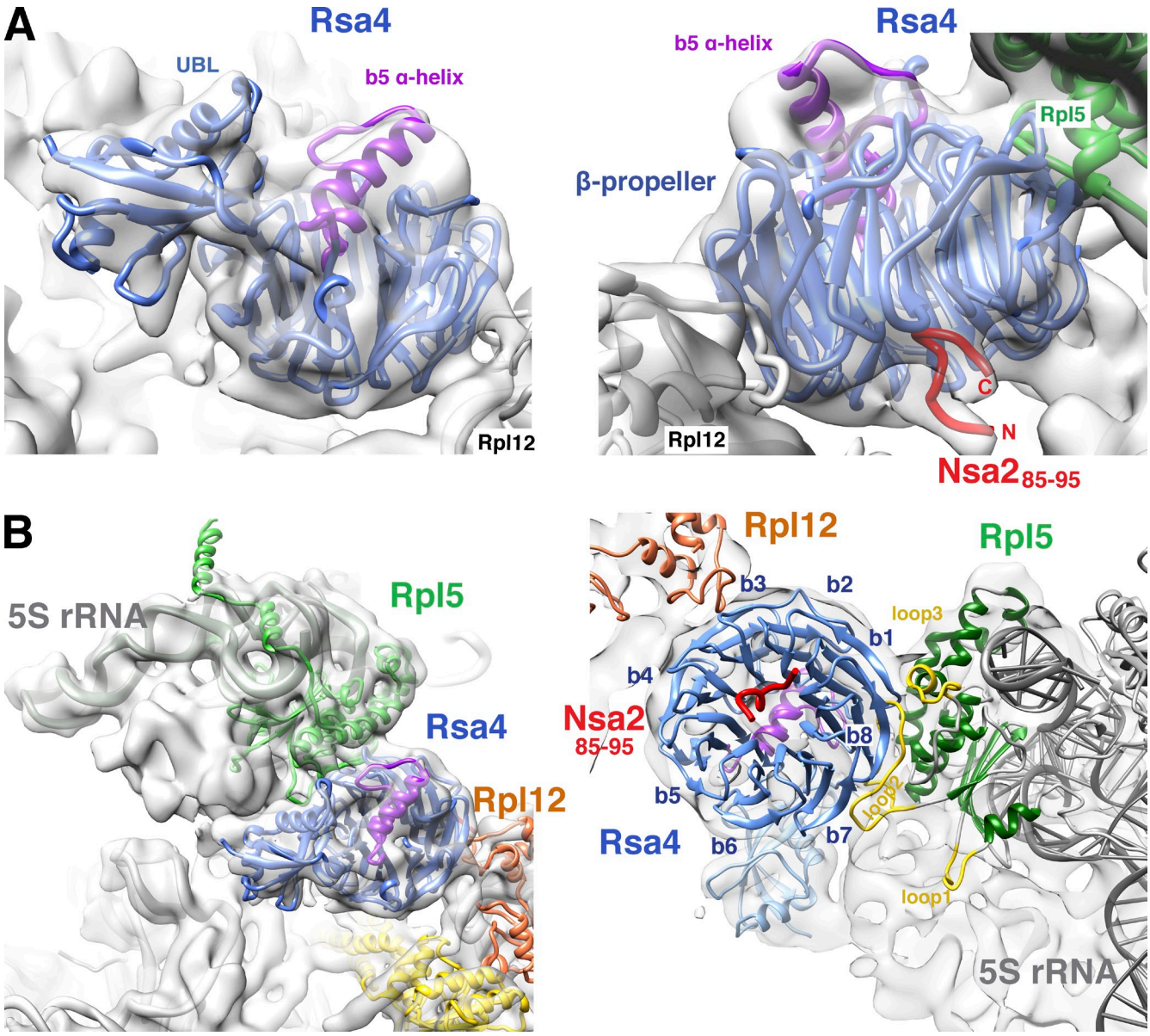

Figure 5. **Contact of Rsa4 to Nsa2, Rpl5 (uL18), and Rpl12 (uL11) on the pre-60S subunit.** The crystal structures of Rsa4 (blue) and the Nsa2 peptide (residues 85–96; red) were fit into the 8.7-Å resolution cryo-EM structure of the Arx1 pre-60S particle. (A) Close view of the electron density of Rsa4 from the subunit joining (left) and solvent site (right). (B) Contact of Rsa4 to neighboring proteins Rpl5 (uL18, green) and Rpl12 (uL11, orange) viewed from the subunit joining site (left) and from the opposite site (right).

cross-linked RNAs in the pre-60S–25S rRNA model confirms that Nsa2 is located under the Rsa4 β-propeller and close to the base of H89 (Fig. 7, B–D). Notably, an unassigned density is observed in the cryo-EM map, leading from the Nsa2 peptide (residues 85–95) to H89 and H42 of the pre-25S rRNA. This density has the dimensions of an ∼15-amino-acid-long α-helix (Fig. 7, B–D). A likely candidate for this extra density is the second, variable α-helix within the Nsa2-N domain (Fig. 3 C, residues 35–60), which is directly connected via a short linker sequence to the Nsa2 peptide (residues 85–95; Fig. S3 D) that is docked at the Rsa4 β-propeller rim. According to this structural model, the first α-helix of Nsa2 (residues 17–32) would bind to rRNA helix 89 in the direct vicinity of the four-helix bundle of the N-domain of Nog1 (Fig. S5 C and Video 1). This is consistent with strong genetic (Fig. S1 A) and two-hybrid interactions that have been reported between Nsa2 and Nog1-N (Lebreton et al., 2006).

We locate the Nsa2 C domain, with its Rps8-like β-barrel fold, to the thus-far unassigned additional EM densities observed between the Rsa4 β-propeller, the four-helix bundle of Nog1, and rRNA helix 89 (see red volume in Fig. 7, B and D). However, a higher resolution of the pre-60S structure is required to allow a precise fit of the Nsa2 C-terminal domain. Nevertheless, our CRAC, NMR, and cryo-EM data clearly indicate that the flexible α-helices of the Nsa2 N domain hook the base of immature H89 and subsequently connect it via Rsa4 to the Rea1 ATPase.

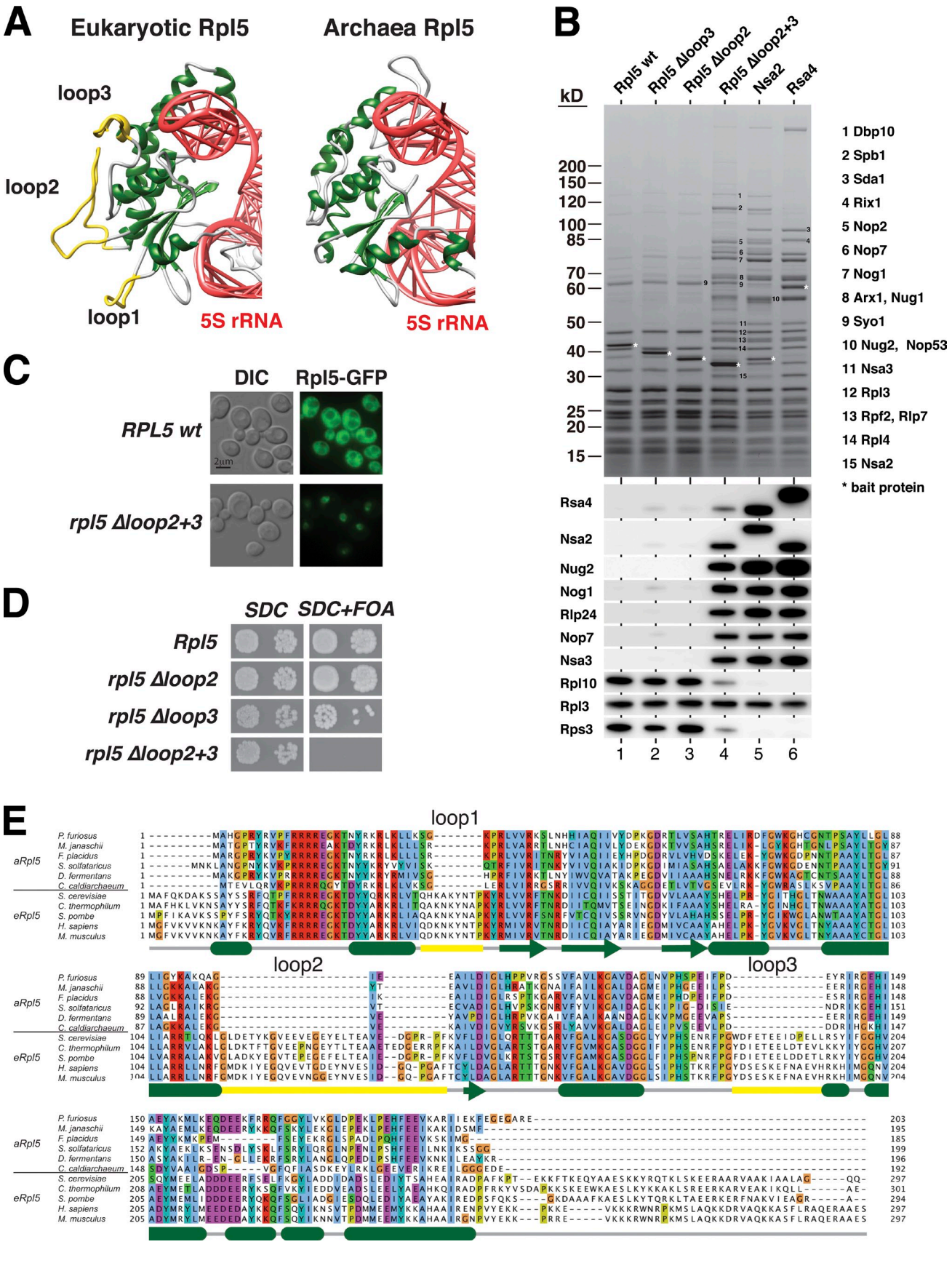

Figure 6. **The eukaryote-specific loops of Rpl5 (uL18) are essential for ribosome biogenesis.** (A) The structure of eukaryotic Rpl5 (uL18, PDB accession no. 3U5I) from *S. cerevisiae* in comparison with archaeal Rpl5 (PDB 3J44). Eukaryote-specific loops are highlighted in yellow; 5S rRNA is shown in red. (B) Affinity purification of Rpl5 wild-type and loop mutant constructs in comparison to other purified bait proteins co-enriched with pre-60S particles.

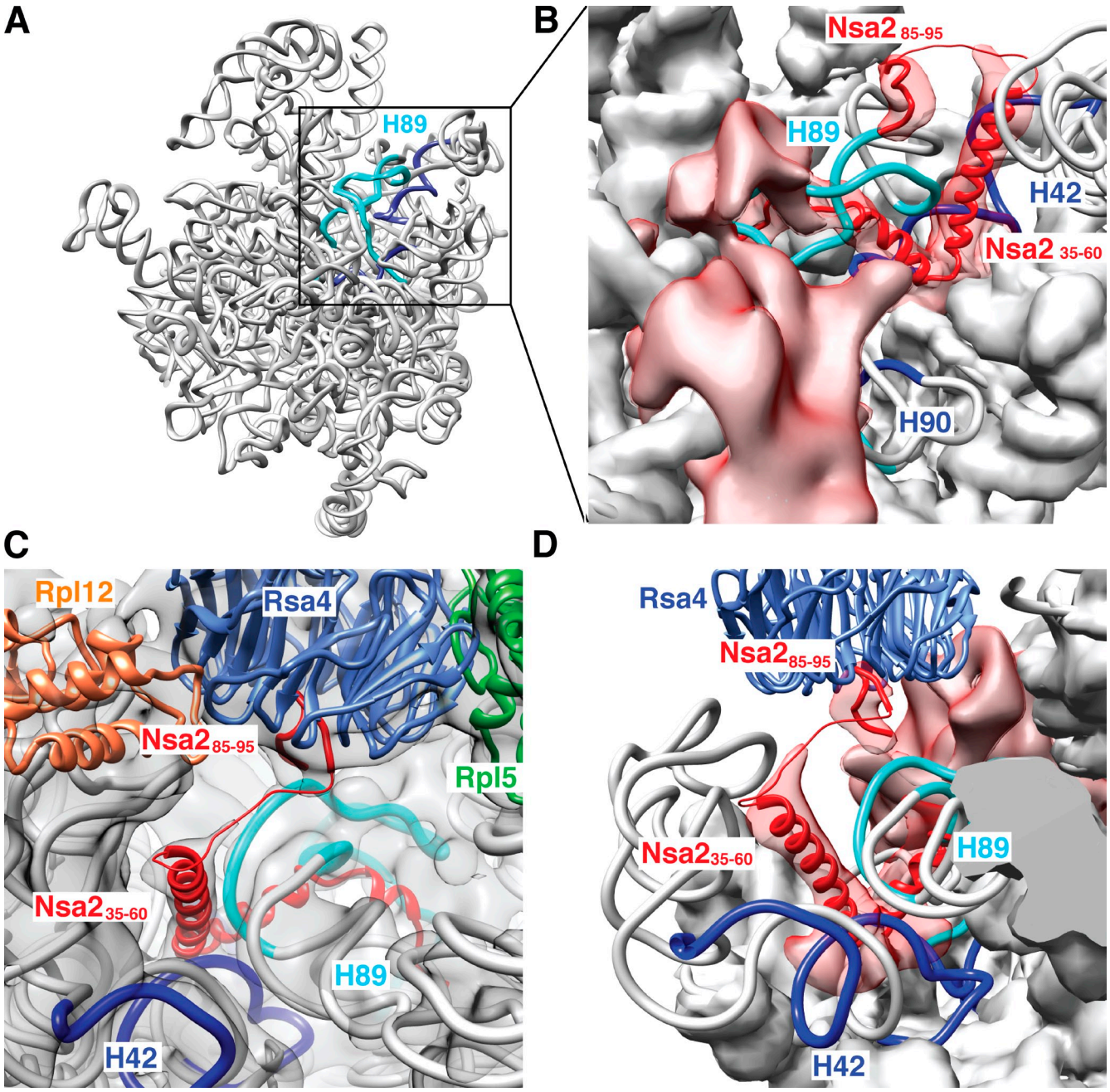

Figure 7. **Nsa2 contacts immature rRNA helix 89 in the pre-60S particle.** (A) Nsa2 cross-linked rRNA fragments are shown in a 3D model of the 25S pre-rRNA (see also Fig. S5). The identified rRNA cross-link sites are highlighted (H89 in light blue; H42 and H90 in dark blue) as an rRNA ribbon present in the Arx1 pre-60S particle. (B and D) Enlarged view of the cross-linked region of the pre-60S particle with fits of the indicated sequences into assigned (Nsa2 residues 85–96; Nsa2 residues 35–60) and unassigned electron densities (volumes colored in red). rRNA is shown as artificial density (8 Å resolution) except for cross-linked H42, H89, and H90, which are depicted as a ribbon model. B is a view from the subunit-joining side, and C and D are from the solvent side. C shows the complete electron density including Rpl12 (uL11, orange), Rpl5 (uL18, green), and Rsa4 (blue) with bound Nsa2 (85–96) peptide (red). From here, unassigned Nsa2 residues (thin red line) connect to a nearby electron density in which $Nsa2_{35–60}$ α-helix is fitted (red). An overview of the complete pre-60S particle including neighbors of the Rsa4–Nsa2 pair is shown in Fig. S5 C.

The indicated Flag-TEV-ProtA (FTpA) Rpl5 proteins were purified from yeast (lanes 1–4) and compared with distinct pre-60S particles affinity-purified via Nsa2-FTpA and FTpA-Rsa4 (lanes 5 and 6). The top panel shows a 4–12% SDS-polyacrylamide gel stained with Coomassie blue, with labeled proteins identified by mass spectroscopy. The bottom panel shows a Western blot analysis of the gel using the indicated antibodies. (C) In vivo localization of Rpl5 Δloop2+3. A wild-type strain was transformed with a plasmid expressing Rpl5-GFP or Rpl5 Δloop2+3-GFP. Fluorescence microcopy was performed to determine their localization. (D) Viability of *rpl5* loop mutants. A *RPL5* shuffle strain was transformed with the indicated *rpl5* alleles. Complementation analysis was done by plating transformants onto SDC+FOA plates. Growth on SDC-LEU plates (SDC) is shown after 3 d, whereas growth on FOA plates is shown after a 5-d incubation at 30°C. (E) Multiple sequence alignment of Rpl5 (uL18) derived from archaea (aRpl5) and eukaryotes (eRpl5). Secondary structure elements of Rpl5 from *S. cerevisiae* are indicated with the same color code as in A.

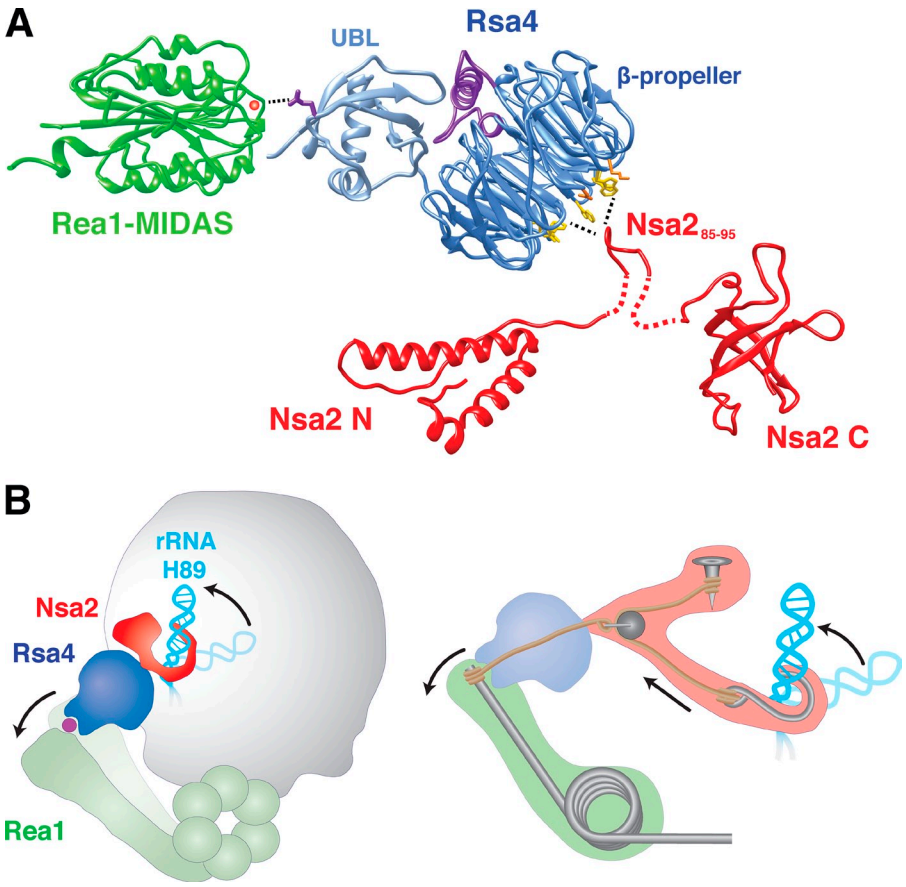

Figure 8. **Model of the factor relay between Nsa2, Rsa4, and the Rea1 MIDAS and its proposed function in rearranging helix 89 toward the PTC.** (A) The depicted Rea1 MIDAS domain (green) carrying a coordinated cation (red ball) is a structural model (modeled with Phyre2, template PDB accession no. 4FX5). The *ct*Rsa4 crystal structure is shown in blue, with conserved E117 orientated toward the MIDAS domain/ion. The Nsa2 N and C domains solved by NMR are shown in red (see also Fig. 3), and the Nsa2 peptide (85–95 aa) in proximity to the top site of the Rsa4 β-propeller with hydrophobic residues is shown in yellow. (B) Illustration of the proposed force relay that transmits mechano-chemical energy from Rea1 through Rsa4 and Nsa2 to helix 89.

Discussion

A combination of structural and functional studies has allowed us to identify a relay network of assembly factors on the pre-60S ribosome surface. This network links the immature PTC, the topologically twisted 5S RNP of the central protuberance, and the emerging P0 stalk with the Rea1 ATPase. The β-propeller of Rsa4 (blade 1 and 8) contacts the twisted 5S RNP via eukaryote-specific loops of Rpl5. In addition, Rsa4 establishes a strong interaction with Nsa2, which is bound to the immature rRNA helix 89. Thus, this network is strategically positioned to receive and transmit mechano-chemical energy generated by the dynein-like Rea1 AAA ATPase into the nascent ribosome. This energy could be exploited to reposition rRNA elements during ribosome biogenesis. We specifically propose that a pulling force on H89 mediated by Nsa2 and Rsa4 participates in the maturation of the PTC, the catalytic center of the ribosome where peptide bond formation occurs. Previous in vitro studies have shown that ATP hydrolysis by Rea1 is required to release Rsa4 from pre-60S particles (Ulbrich et al., 2009; Matsuo et al., 2014), which indicates that Rea1 utilizes ATP hydrolysis to generate energy that is transmitted to Rsa4. Importantly, Nsa2 is not released during this in vitro maturation step (Ulbrich et al., 2009; Matsuo et al., 2014). We consider these previous findings and the data from this study to propose the following multiple-step mechanism in which Rea1, Rsa4, and Nsa2 participate in a coordinated action (Fig. 8): (1) the MIDAS domain of Rea1 binds to the UBL domain of Rsa4; (2) ATP hydrolysis generates a power stroke that pulls on Rsa4; and (3) this energy is transmitted via the Rsa4 β-propeller and its binding partner Nsa2 toward rRNA helix 89 to facilitate rRNA relocation. During this rearrangement, the Nsa2 C domain, which is bound at a nearby site (see red volume in Fig. 7, B and D), could serve as a binding site on the preribosome. (4) During or after these remodeling steps, the Rsa4–Nsa2 interaction breaks, leading to the complete detachment of Rsa4 from the pre-60S particle, and (5) Nsa2 is released from the preribosome in a subsequent step by a yet-unknown mechanism. Because the GTPase Nog1 also contacts rRNA helix 89 with its N-terminal domain and has a strong functional link to Rsa4 and Nsa2 (Fig. S1), we assume that Nog1 and possibly other factors also participate in the relocation of helix 89, required for forming the active PTC.

Interestingly, the Rea1 AAA ATPase has additional substrates at earlier biogenesis steps (Baßler et al., 2010). Like Rsa4, Ytm1 has a predicted UBL-like domain that directly interacts with Rea1. Moreover, Ytm1 is also released from pre-60S particles in a Rea1-dependent manner. Ytm1 is part of the Nop7–Erb1–Ytm1 complex (called the PeBoW complex in humans; Miles et al., 2005; Rohrmoser et al., 2007; Tang et al., 2008) that binds closely to ITS2 (Granneman et al., 2011), which is the intervening sequence between the 5.8S and 25S rRNA. Analogous to the Rsa4–Nsa2 relay, the Ytm1 complex could transmit remodeling energy toward ITS2, which is known to undergo structural rearrangement during maturation (Côté et al., 2002; Granneman et al., 2011). Thus, different assembly

factor networks may harness the energy generated by Rea1-mediated ATP hydrolysis to remodel both rRNA and protein components of the nascent ribosome.

Materials and methods

Yeast and bacterial methods

Yeast strains (Table 1) were grown in yeast extract peptone dextrose (YPD) or selective SDC medium (SD + CSM supplement). *Escherichia coli* strains were grown in lysogeny broth (LB) medium. Transformations were performed according to standard protocols. Plasmids used in this study are listed in Table 2. Generation of yeast double shuffle strains and genetic analyses were performed according to published procedures (Strässer et al., 2000). Antibodies used for Western blot analysis were obtained from M. Fromont-Racine (Institut Pasteur, Paris, France), A. Johnson (University of Texas, Austin, TX), V. Panse (ETH, Zürich, Switzerland), M. Seedorf (Zentrum für Molekulare Biologie der Universität Heidelberg, Heidelberg, Germany), D. Wolf (Universität Stuttgart, Stuttgart, Germany), and M. Remacha (Centro de Biologia Molecular Severo Ochoa, Madrid, Spain). TAP-Rsa4 (2× ProtA-TEV-CBP-Flag-Rsa4) was generated by homologous recombination of the PCR product generated from pnatNT2-P_{RSA4}-NTAP-Flag. Arx1-FTpA (Arx1-Flag-TEV-ProtA), Nsa2-HTpA (Nsa2-His6-TEV-ProtA) was generated by homologous recombination using integration cassettes. Nsa2-FTpA was done accordingly, with specific primers that insert a linker sequence (ASSYTAPQPGLGGS) between *NSA2* and the FTpA tag.

For TAP purification, a pellet of a 2-liter yeast culture was lysed and centrifuged. The supernatant was bound to IgG-Sepharose (GE Healthcare) for 90 min, washed, and eluted by incubation with tobacco etch virus (TEV) protease for 120 min. Eluate was further affinity purified by binding to FLAG beads (Sigma-Aldrich) for 45 min, washed, and eluted with FLAG peptide to reduce contamination to a minimum. For detailed description, see Bradatsch et al. (2012).

The CRAC method of cross-linking biogenesis factors to RNA has been applied according to Granneman et al. (2009). A yeast culture was treated with UV to cross-link proteins to RNA. Harvested cells were lysed using zirconia beads, and Nsa2-His-TEV-protA was purified using IgG-Sepharose (GE Healthcare). The TEV eluate was treated with RNases and denatured, and Nsa2 was purified under denaturating conditions using NiNTA beads. Cross-linked RNA was ligated to 3′ and 5′ DNA linker and sequenced.

The yeast two-hybrid analysis was done according to James et al. (1996). The yeast two-hybrid strain PJ69-4a was transformed with the indicated Nsa2 (pASΔΔ) and Rsa4 (pG4ADHAN) constructs expressing Gal4-DNA-BD-NSA2 and Gal4-AD-RSA4 (see Table 2) and plated on SDC-TRP-LEU medium. A positive interaction is monitored by growth on SDC-TRP-LEU-HIS and SDC-TRP-LEU-ADE medium.

Cells for sucrose gradient analysis were grown to OD 0.6–0.8, treated with cycloheximide for 15 min, and lysed by vortexing with glass beads for 4 × 30 s. The cleared lysates were applied on 10–50% sucrose gradients and spun for 16 h at 27,000 rpm in a SW40 rotor (Beckman). Profile recording at 254 nm and fractionation (0.4 ml) was done using "Foxy junior" from Isco with Peak TRAK software. The detailed protocol is described in Baßler et al. (2001).

Microscope imaging

Cells, expressing plasmid-borne GFP- and RFP-tagged proteins, were grown to ∼OD 0.5 in liquid culture using a selective medium at 30°C. Before microscopy, cells were harvested by centrifugation and washed with water. Subsequent fluorescence microscopy was performed at room temperature using a microscope (Imager Z1; Carl Zeiss) with a 100×, NA 1.4 Plan-Apochromat oil immersion objective lens (Carl Zeiss) and a DICIII, HE-EGFP, or HE-Cy3 filter set. Pictures were acquired with a camera (AxioCamMRm) and AxioVision 4.8.2.0 software (both from Carl Zeiss) at a resolution of 1,388 × 1,040 (binning 1 × 1, gain factor 1). Pictures were exported as TIF files and processed in Photoshop CS 6 (Adobe) for levels. The detailed procedure to localize GFP- and RFP-tagged proteins using fluorescence microscopy has been described in Bassler et al. (2006).

Nonradioactive pulse-chase labeling combined with affinity purification of ribosomal Rpl25

The yeast strain DS1-2b was transformed with pEcOmeTyr/ectRNA$_{CUA}$ (carrying the amber [TAG] suppressor tRNA and its corresponding tRNA synthetase; Chin et al., 2003) and YEplac181 $P_{GAL1\text{-}10}$ *NSA2* $P_{GAL1\text{-}10}$ tc-apt-2×*HA*-TAG-*RPL25-FTpA* for *GAL*-inducible overexpression of Rpl25-FTpA and Nsa2 (wild type or Y90A mutant). Expression of *GAL::NSA2* and HA-Rpl25-FTpA mRNA was induced for 60 min by the addition of galactose. Then, the translation of HA-Rpl25-FTpA was pulsed for 7 min by the addition of *O*-methyl-tyrosine and subsequently chased for 20 min by the addition of tetracycline and glucose. For subsequent analysis, Rpl25 was purified using the standard TAP protocol (see above). The eluates were analyzed by SDS-PAGE on 4–12% NuPAGE gels. Associated proteins were identified by mass spectrometry. For details see Stelter et al. (2012) and Stelter and Hurt (2014).

Generation of temperature-sensitive *nsa2* and *ipi3* mutants

Temperature-sensitive *nsa2* and *ipi3* mutants were generated by PCR-based random mutagenesis (Santos-Rosa et al., 1998; Baßler et al., 2001). Accordingly, the genes were amplified with Taq DNA polymerase (Invitrogen) according to the manufacturer's instructions, except for a 0.2 mM final $MgCl_2$ concentration, 10% DMSO, and, in each of four separate reactions, one dNTP concentration reduced from 2.5 mM to 0.5 mM final concentration. Reactions were pooled, then cloned with SacI–XhoI into pRS314 for Nsa2 or XmaI–SpeI into pRS315 for Ipi3. The obtained library was transformed into yeast shuffle strains, incubated on FOA plates. Temperature-sensitive phenotype was tested by replica plating at 23°C, 30°C, and 37°C. Plasmid DNA was recovered, sequenced, and retransformed to confirm the *ts* phenotype.

Recombinant protein expression and purification

Purified proteins used in binding assays, ITC, and crystallization of *sc*Rsa4 and the *sc*Nsa2–*sc*Rsa4 complex were produced in BL21 codon plus (DE3) cells (EMD Millipore) by IPTG induction for 3 h. All *E. coli* cells were lysed with a microfluidizer (Microfluidics). All fusion proteins were purified in batches with the respective affinity resins.

MBP-scNsa2 fusion proteins. Frozen *E. coli* pellets were resuspended in $NaCl_{200}$ buffer (20 mM Hepes, pH 7.5, 200 mM NaCl, and 1 mM DTT). The cleared lysate was incubated with SP Sepharose (Sigma-Aldrich) for 1 h to reduce ribosomal contamination. After extensive washing ($NaCl_{200}$), MBP-scNsa2 was eluted with $NaCl_{600}$ buffer (20 mM Hepes, pH 7.5, and 600 mM NaCl). The eluates were incubated with Amylose Resin (New England Biolabs, Inc.) for 1 h. After extensive washing ($NaCl_{200}$), the beads were resuspended in $NaCl_{200}$ buffer and used for binding assays. MBP control and MBP-scNsa2 peptide were purified accordingly, without the SP Sepharose step.

HIS-TEV-scRsa4 fusion proteins. Frozen pellets were resuspended in $NaCl_{200}$ buffer (20 mM Hepes, pH 7.5, 200 mM NaCl, and 1 mM DTT). After lysis, imidazole, pH 8.0, was added to a final concentration of 10 mM. The clarified lysate was then incubated with NiNTA (Macherey-Nagel) for 1 h. After extensive washing ($NaCl_{200}$), the fusion proteins were eluted with $NaCl_{200}$ buffer containing 200 mM imidazole.

In vitro reconstitution of the Rsa4–Nsa2 interaction. Binding assays were performed using Micro Bio-Spin columns (Bio-Rad Laboratories). To reduce nonspecific binding, *E. coli* lysate was used as a competitor. Because *E. coli* express endogenous MBP, the lysate was depleted of MBP with Amylose Resin before use.

For binding studies, MBP-bait proteins bound to Amylose Resin were incubated with a 5× excess of Rsa4 variants mixed with *E. coli* lysate. After 45 min of incubation, the beads were washed with buffer $NaCl_{200}$ (20 mM Hepes, pH 7.5, 200 mM NaCl, and 1 mM DTT). Bound proteins were eluted by incubating the beads for 10 min at 65°C with SDS sample buffer.

For binding assays of scNsa2 deletion constructs, GST-Nsa2 and HIS-Rsa4 were coexpressed. Frozen pellets were resuspended in buffer $NaCl_{250}$ (20 mM Hepes, pH 7.5, 250 mM NaCl, and 0.01% NP-40). The clarified lysate was incubated with Glutathione Sepharose Resin (Macherey-Nagel) for 1 h. After extensive washing ($NaCl_{250}$), the beads were resuspended in $NaCl_{250}$ buffer + 1 mM DTT. Bound proteins were released by TEV cleavage (1 h), and the samples were precipitated with TCA.

ITC measurement. Frozen pellets expressing *sc*Rsa4 Δ136 were resuspended in buffer $NaCl_{50}$ (20 mM Hepes, pH 7.5, 50 mM NaCl, and 1 mM DTT). The cleared lysate was bound to SP Sepharose (Sigma-Aldrich). After extensive washing, *sc*Rsa4Δ136 was eluted with $NaCl_{200}$ buffer (20 mM Hepes, pH 7.5, 200 mM NaCl, and 1 mM DTT). The eluate was concentrated and subjected to size-exclusion chromatography (SEC) using a HiLoad 16/60 Superdex200 column (GE Healthcare) equilibrated in gel filtration buffer (20 mM Hepes, pH 7.5, 200 mM NaCl, and 1 mM DTT). Peak fractions of *sc*Rsa4Δ136 and the *sc*Nsa2 peptide (residues 85–95: DALPTYLLDRE; PSL GmbH) were dialyzed overnight at 4°C against ITC buffer (20 mM Hepes, pH 7.5, 200 mM NaCl, and 1 mM TCEP). ITC experiments were performed using a VP-ITC microcalorimeter (MicroCal) at 25°C. All samples were degassed before titration. Titrations consisted of 23 injections of 12-µl aliquots (300 µM of Nsa2 peptide) with 300-s

intervals into the cell solution (30 µM Rsa4ΔN136). Data processing was performed with the Origin 7.0 software.

Crystallization of the minimal Rsa4–Nsa2 complex. For crystallization of the minimal *sc*Rsa4–*sc*Nsa2 complex, *sc*Nsa2 (81–101 aa) was recombinantly expressed as an MBP fusion protein and incubated with *sc*Rsa4Δ136. To facilitate crystallization, the original MBP sequence was mutated according to Moon et al. (2010) to reduce surface entropy (see also Table 2). MBP-scNsa2 was bound to Amylose Resin for 1 h and mixed with lysate from cells containing *sc*Rsa4Δ136. After 1 h of incubation time and washing, the complex was eluted with 10 mM maltose. It was then subjected to SEC using a HiLoad 16/60 Superdex200 column (GE Healthcare) equilibrated in gel filtration buffer (20 mM Hepes, pH 7.5, 200 mM NaCl, and 1 mM DTT). Peak fractions were pooled and concentrated to a final concentration of 46 mg/ml. Crystals were grown at 18°C in hanging drops containing 2 µl of MBP-scNsa2–scRsa4Δ136 complex and 0.5 µl of a reservoir solution consisting of 200 mM NH_4SO_4 and 20% polyethylene glycol (PEG) 3350. After 57 d, needle-shaped crystals were discovered.

Crystallization of *sc*Rsa4. Plasmid pT7 HIS-TEV-*sc*Rsa4ΔN26 expressing *sc*Rsa4 (27–515) was transformed into *E. coli* strain BL21. Preculture (LB) was grown overnight to be inoculated in 10 liters of LB medium with OD 0.05–0.1. At OD 0.6–0.7, IPTG was added to a final concentration of 0.2 mM, and cells were shifted to 23°C for 2 h. Rsa4 was affinity purified with NiNTA resin (buffer 150 mM NaCl, 50 mM Tris, pH 7.5, 5 mM $MgCl_2$, 10 mM imidazole, 0.1% Tween, and 10% glycerol) and eluted by 150 mM imidazole (150 mM NaCl and 50 mM Tris, pH 7.5). Eluted protein was dialyzed overnight in the presence of TEV protease, TEV was removed by incubation with NiNTA beads, and flow-through was concentrated and further purified by SEC using a Superdex200 16/60 (GE Healthcare). Purified *sc*Rsa4 was concentrated to 170–210 mg/ml and crystallized at 25°C in hanging drops containing 0.4 µl of protein and 0.4 µl buffer reservoir solution consisting of 3.5 M $NaHCO_2$ and 2.25 M NH_4Ac.

Crystallization of *ct*Rsa4. Because *ct*Rsa4 was insoluble upon expression in *E. coli*, we produced *ct*Rsa4 in yeast. Yeast strain DS1-2b was transformed with pADH181 *pA-TEV-ctrsa4*Δ1–29 to express *ct*Rsa4 (residues 27–517). A preculture (SRC-Leu) grown overnight was used to inoculate 12 liters of YPG with OD 0.2. Culture was harvested after 16 h with an OD of 4–4.5. Cells were lysed in a cryo mill (MM400, Retsch) in a buffer of 150 mM NaCl, 50 mM Tris, pH 7.5, 1.5 mM $MgCl_2$, and 0.15% NP-40. *ct*Rsa4 was affinity-purified using IgG Sepharose (GE Healthcare), washed with buffer including 50 mM ATP, a high-salt buffer (500 mM NaCl, 50 mM Tris, pH 7.5, 1.5 mM $MgCl_2$, and 0.15% NP-40). Protein was eluted by TEV cleavage in 100 mM NaCl buffer, concentrated, and loaded on a Superdex 200 16/60 (50 mM NaCl). Purified *ct*Rsa4 was concentrated to 22 mg/ml and crystallized at 18°C in hanging drops containing 0.4 µl of protein and 0.4 µl of buffer (0.2 mM KF and 20% PEG 3350).

NMR data collection and analysis

All NMR data were acquired at 7°C on 0.45 mM of uniformly labeled (^{13}C and ^{15}N, or ^{15}N) *ct*Nsa2 residues 168–261 and *ct*Nsa2 residues 1–84 prepared in 10 mM Tris-HCl buffer, pH 7.4, containing 5 mM NaCl, 2 mM TCEP, 10% D_2O, a protease inhibitor cocktail (Roche), and 1 mM 2, 2-dimethylsilapentene-5-sulfonic acid for proton referencing. A standard set of 2D (^{15}N or ^{13}C-HSQC) and 3D triple resonance experiments (HNCO, HN(CA)CO, HNCACB, and CBCA(CO)NH; 3D HBHA(CO)NH, 3D H(CCCO)NH, (H)CC(CO)NH, and HCCH-TOCSY; Sattler et al., 1999) for backbone and side chain assignments were acquired on 600 or 850 MHz Bruker Avance III spectrometers equipped with a cryogenic $^1H/^{13}C/^{15}N$ QCI or TCI probe heads with z axis gradients. ^1H-^1H distance restraints for structure calculation were obtained from 3D-edited (^{13}C, ^{15}N) NOESY-HSQC experiments acquired on a Bruker Avance III 950 MHz spectrometer. The edited experiments were recorded with a mixing time of 120 ms. Hydrogen bond restraints were obtained from hydrogen/deuterium (H/D) exchange experiments. In brief, a series of ^{15}N HSQC data were collected over a period of time on a lyophilized protein dissolved in D_2O. Amide protons were considered to be involved in hydrogen bonding if they were still visible in the HSQC spectrum after the first HSQC experiment. Two distance restraints applied for $H^N(i)$-O(j) and N(i)-O(j) were used as hydrogen bond constraints in structure calculations. All NMR data were processed with NMRPipe/NMR-Draw 5.5 (Delaglio et al., 1995), and analyzed with the graphical NMR assignment and integration software Sparky 3.115 (Goddard and Kneller, 2008).

NMR structure calculation

Data input for structure calculations of Nsa2-C (168–261 aa) were based on information from resonance assignments, and peaks from ^{13}C- and ^{15}N-edited NOESY spectra were picked with the automated peak picking software PONDEROSA (Lee et al., 2011). The picked peaks were used as input for a series of CYANA (Güntert, 2004) structure calculations, which combines H-H distance restraints data with dihedral angle restraints derived from TALOS+ (Shen et al., 2009) and hydrogen bonds restraints from H/D exchange experiments to generate an ensemble of 20 energy-minimized conformers. The automated structures generated by CYANA were used along with the assigned peaks to further refine the structures. The quality of the structure was checked with the Protein Structure Validation Software (PSVS) server. For Nsa2-N (1–84 aa), structure determination used CS-Rosetta, a chemical-shift–based method for structure determination (Shen et al., 2008) that uses chemical shift assignments for the $^1H_\alpha$, ^1H_N, $^{13}C_\alpha$, $^{13}C_\beta$, $^{13}C'$, and ^{15}N atoms. 3,000 structures were generated and 20 low-energy structures were selected for analysis, all of which exhibited similarity in the length of the two main α-helices (residues 5–33 and 38–60), and variability in their packing against each other. The large deviation is attributed to the high level of disorder in the loops connecting the helices.

X-ray data collection and structure determination

Crystals were cryoprotected in mother liquor containing 20% (vol/vol) ethylene glycol or glycerol and flash-cooled in liquid nitrogen. Diffraction data were collected under cryogenic conditions (100 K) on beamline ID14-4 and ID23-1 at the European Synchrotron Radiation Facility (ESRF). X-ray diffraction data were processed and scaled using xds and scala (Collaborative Computational Project, Number 4, 1994; Kabsch, 2010).

***ct*Rsa4 Crystals of *ct*Rsa4 belong to space group P1 and contain one molecule in the asymmetric unit.** The structure was solved by molecular replacement with the program PHASER (McCoy et al., 2007) using an eight-bladed β-propeller domain as a search model (Protein Data Base [PDB] accession no. 1NEX; Orlicky et al., 2003). Initial model building was performed with the Phenix program suite (Adams et al., 2010) and Buccaneer (Cowtan, 2006). The protein model was refined using Phenix and iterative model building in COOT (Emsley et al., 2010), including TLS refinement at the last stage of refinement. Ramachandran statistics for the final model of *ct*Rsa4 show 96.5% of residues in the most favorable regions, 3.5% in allowed regions, and 0% in disallowed regions according to MolProbity (Chen et al., 2010).

***sc*Rsa4.** Crystals of *sc*Rsa4 belong to space group I222 and contain two molecules in the asymmetric unit. The structure was solved by molecular replacement with the program PHASER (McCoy et al., 2007) using *ct*Rsa4 as a search model. Initial model building was performed with the Phenix program suite (Adams et al., 2010) and Buccaneer (Cowtan, 2006). The protein model was refined using Phenix (Adams et al., 2010), and iterative model building was done with COOT (Emsley et al., 2010). Ramachandran statistics for the final model of *sc*Rsa4 show 90.5% of residues in the most favorable regions, 7.5% in allowed regions, and 2% in disallowed regions according to MolProbity (Chen et al., 2010).

***sc*Rsa4–MBP–*sc*Nsa2.** Crystals of *sc*Rsa4–MBP-*sc*Nsa2 belong to space group C2 and contain four molecules in the asymmetric unit. The structure was solved by molecular replacement with the AutoMR program of the Phenix program suite (Adams et al., 2010) using the β-propeller domain of *sc*Rsa4 and MBP as a search model (PDB code 4EDQ). The protein model was refined using Phenix (Adams et al., 2010) and iterative model building was done using COOT (Emsley et al., 2010). Ramachandran statistics for the final model of *sc*Rsa4–MBP–*sc*Nsa2 show 96.2% of residues in the most favorable regions, 3.7% in allowed regions, and 0.1% in disallowed regions according to MolProbity (Chen et al., 2010).

Accession numbers

Crystal and NMR structures have been deposited to the PDB database with following accession numbers: *ct*Rsa4 (4WJS), *sc*Rsa4 (4WJU), *sc*Rsa4–scNsa2 (4WJV), and *ct*Nsa2-C (2MVF); and to the Biological Magnetic Resonance Data Bank database with accession numbers *ct*Nsa2-C (25265) and *ct*Nsa2-N (25264).

Online supplemental material

Fig. S1 shows that *RSA4* interacts with *NSA2* genetically and in Y2H assays. Fig. S2 presents the crystal structures of scRsa4 and scRsa4–scNsa2 complex shown in ribbon representation. Fig. S3 demonstrates that the overexpressed nsa2 Y90A mutant blocks 60S biogenesis. Fig. S4 elucidates the phenotype of different *rsa4* mutants. Fig. S5 shows that CRAC analysis reveals the binding sites of Nsa2 to the 25S rRNA helices of the PTC. Video 1 illustrates the molecular fit of the Rsa4 (PDB accession no. 4WJS) and Nsa2 structures (PDB accession no. 4WJV), as well as a model of Nsa2-N derived from BMRB 25264, into the Arx1 particle and the interpolated

movement of helix 89 in maturation of the PTC from the Arx1-particle to the mature 60S subunit. Online supplemental material is available at http://www.jcb.org/cgi/content/full/jcb.201408111/DC1.

We thank C. Leidig, G. Manikas, Y. Matsuo, B. Bradatsch, E. Thomson, and C. Ulbrich for reagents and discussion on the project. We thank R. Kunze for purification of pulse-chased Rpl25; C. Ulbrich and M. Haufe for the genetic analysis; S. Bilen for generation of the *ipi3* ts mutants; G. Manikas for cloning of *ctRSA4;* K. Wild, Y. Ahmed, E. Lenherr, and D. Lupo for support in crystallization and data collection; and J. Kopp and C. Siegmann from the BZH/Cluster of Excellence CellNetworks crystallization platform for protein crystallization. We are grateful to D. Kressler, M. Fromont-Racine, A. Johnson, V. Panse, M. Seedorf, D. Wolf, and M. Remacha for sharing plasmids, strains, and antibodies; to J. Nováček and R. Fiala of the National Center for Biomedical Research (Faculty of Science) Masaryk University for NMR data collection; and to W. Lee at National Magnetic Resonance Facility at Madison for access to PONDEROSA before its publication.

J. Baßler and E. Hurt are supported by grants from Deutsche Forschungsgemeinschaft (DFG; BA2316/1-4, HU363/10-5). E. Barbar and A. Nyarko are supported by the National Institutes of Health (GM 084276). I. Sinning acknowledges support by grants from DFG (FOR967, GRK1188, and SFB638). I. Sinning and E. Hurt are investigators of the cluster of excellence CellNetworks. Financial support from the Access to Research Infrastructures activity in the seventh Framework Program of the European Community (Project number 261863, Bio-NMR) for conducting the research is also acknowledged. C. Barrio-Garcia is a fellow of the Graduiertenkolleg GRK 1721.

The authors declare no further competing financial interests.

Author contributions: J. Baßler and E. Hurt designed the research, and J. Baßler, H. Paternoga, M. Thoms, I. Holdermann, S. Granneman, A. Nyarko, S.A. Clark, G. Stier, D. Schraivogel, and M. Kallas performed experiments. J. Baßler, H. Paternoga, and M. Kallas crystallized proteins. I. Holdermann, and I. Sinning determined and analyzed the crystal structures. NMR analysis was done by A. Nyarko, S.A. Clark, and E. Barbar. In vitro binding assays were done by H. Paternoga, and M. Thoms did the Rpl5 experiments. J. Baßler did the sucrose gradient analysis, S. Granneman did the CRAC experiment, and S. Granneman and D. Tollervey analyzed data. J. Baßler, H. Paternoga, M. Thoms, C. Barrio-Garcia, E. Hurt, and R. Beckmann interpreted EM data. J. Baßler and E. Hurt wrote the manuscript.

Submitted: 27 August 2014
Accepted: 16 October 2014

References

Adams, P.D., P.V. Afonine, G. Bunkóczi, V.B. Chen, I.W. Davis, N. Echols, J.J. Headd, L.W. Hung, G.J. Kapral, R.W. Grosse-Kunstleve, et al. 2010. PHENIX: a comprehensive Python-based system for macromolecular structure solution. *Acta Crystallogr. D Biol. Crystallogr.* 66:213–221. http://dx.doi.org/10.1107/S0907444909052925

Bassler, J., M. Kallas, and E. Hurt. 2006. The NUG1 GTPase reveals an N-terminal RNA-binding domain that is essential for association with 60 S preribosomal particles. *J. Biol. Chem.* 281:24737–24744. http://dx.doi.org/10.1074/jbc.M604261200

Baßler, J., P. Grandi, O. Gadal, T. Lessmann, E. Petfalski, D. Tollervey, J. Lechner, and E. Hurt. 2001. Identification of a 60S preribosomal particle that is closely linked to nuclear export. *Mol. Cell*. 8:517–529. http://dx.doi.org/10.1016/S1097-2765(01)00342-2

Baßler, J., M. Kallas, B. Pertschy, C. Ulbrich, M. Thoms, and E. Hurt. 2010. The AAA-ATPase Rea1 drives removal of biogenesis factors during multiple stages of 60S ribosome assembly. *Mol. Cell*. 38:712–721. http://dx.doi.org/10.1016/j.molcel.2010.05.024

Ben-Shem, A., N. Garreau de Loubresse, S. Melnikov, L. Jenner, G. Yusupova, and M. Yusupov. 2011. The structure of the eukaryotic ribosome at 3.0 Å resolution. *Science*. 334:1524–1529. http://dx.doi.org/10.1126/science.1212642

Bradatsch, B., C. Leidig, S. Granneman, M. Gnädig, D. Tollervey, B. Böttcher, R. Beckmann, and E. Hurt. 2012. Structure of the pre-60S ribosomal subunit with nuclear export factor Arx1 bound at the exit tunnel. *Nat. Struct. Mol. Biol.* 19:1234–1241. http://dx.doi.org/10.1038/nsmb.2438

Chantha, S.C., and D.P. Matton. 2007. Underexpression of the plant NOTCHLESS gene, encoding a WD-repeat protein, causes pleitropic phenotype during plant development. *Planta*. 225:1107–1120. http://dx.doi.org/10.1007/s00425-006-0420-z

Chen, V.B., W.B. Arendall III, J.J. Headd, D.A. Keedy, R.M. Immormino, G.J. Kapral, L.W. Murray, J.S. Richardson, and D.C. Richardson. 2010. MolProbity: all-atom structure validation for macromolecular crystallography. *Acta Crystallogr. D Biol. Crystallogr.* 66:12–21. http://dx.doi.org/10.1107/S0907444909042073

Chin, J.W., T.A. Cropp, J.C. Anderson, M. Mukherji, Z. Zhang, and P.G. Schultz. 2003. An expanded eukaryotic genetic code. *Science*. 301:964–967. http://dx.doi.org/10.1126/science.1084772

Collaborative Computational Project, Number 4. 1994. The CCP4 suite: programs for protein crystallography. *Acta Crystallogr. D Biol. Crystallogr.* 50:760–763. http://dx.doi.org/10.1107/S0907444994003112

Côté, C.A., C.L. Greer, and B.A. Peculis. 2002. Dynamic conformational model for the role of ITS2 in pre-rRNA processing in yeast. *RNA*. 8:786–797. http://dx.doi.org/10.1017/S1355838202023063

Cowtan, K. 2006. The Buccaneer software for automated model building. 1. Tracing protein chains. *Acta Crystallogr. D Biol. Crystallogr.* 62:1002–1011. http://dx.doi.org/10.1107/S0907444906022116

Delaglio, F., S. Grzesiek, G.W. Vuister, G. Zhu, J. Pfeifer, and A. Bax. 1995. NMRPipe: a multidimensional spectral processing system based on UNIX pipes. *J. Biomol. NMR*. 6:277–293. http://dx.doi.org/10.1007/BF00197809

Emsley, P., B. Lohkamp, W.G. Scott, and K. Cowtan. 2010. Features and development of Coot. *Acta Crystallogr. D Biol. Crystallogr.* 66:486–501. http://dx.doi.org/10.1107/S0907444910007493

Fromont-Racine, M., B. Senger, C. Saveanu, and F. Fasiolo. 2003. Ribosome assembly in eukaryotes. *Gene*. 313:17–42. http://dx.doi.org/10.1016/S0378-1119(03)00629-2

Galani, K., T.A. Nissan, E. Petfalski, D. Tollervey, and E. Hurt. 2004. Rea1, a dynein-related nuclear AAA-ATPase, is involved in late rRNA processing and nuclear export of 60 S subunits. *J. Biol. Chem.* 279:55411–55418. http://dx.doi.org/10.1074/jbc.M406876200

Goddard, T.D., and D.G. Kneller. 2008. Sparky - NMR Assignment and Integration Software. University of California, San Francisco. Last revised May 30, 2008. https://www.cgl.ucsf.edu/home/sparky/ (accessed October 29, 2014).

Granneman, S., G. Kudla, E. Petfalski, and D. Tollervey. 2009. Identification of protein binding sites on U3 snoRNA and pre-rRNA by UV cross-linking and high-throughput analysis of cDNAs. *Proc. Natl. Acad. Sci. USA*. 106:9613–9618. http://dx.doi.org/10.1073/pnas.0901997106

Granneman, S., E. Petfalski, A. Swiatkowska, and D. Tollervey. 2010. Cracking pre-40S ribosomal subunit structure by systematic analyses of RNA-protein cross-linking. *EMBO J.* 29:2026–2036. http://dx.doi.org/10.1038/emboj.2010.86

Granneman, S., E. Petfalski, and D. Tollervey. 2011. A cluster of ribosome synthesis factors regulate pre-rRNA folding and 5.8S rRNA maturation by the Rat1 exonuclease. *EMBO J.* 30:4006–4019. http://dx.doi.org/10.1038/emboj.2011.256

Güntert, P. 2004. Automated NMR structure calculation with CYANA. *Methods Mol. Biol.* 278:353–378.

Henras, A.K., J. Soudet, M. Gérus, S. Lebaron, M. Caizergues-Ferrer, A. Mougin, and Y. Henry. 2008. The post-transcriptional steps of eukaryotic ribosome biogenesis. *Cell. Mol. Life Sci.* 65:2334–2359. http://dx.doi.org/10.1007/s00018-008-8027-0

Honma, Y., A. Kitamura, R. Shioda, H. Maruyama, K. Ozaki, Y. Oda, T. Mini, P. Jenö, Y. Maki, K. Yonezawa, et al. 2006. TOR regulates late steps of ribosome maturation in the nucleoplasm via Nog1 in response to nutrients. *EMBO J.* 25:3832–3842. http://dx.doi.org/10.1038/sj.emboj.7601262

James, P., J. Halladay, and E.A. Craig. 1996. Genomic libraries and a host strain designed for highly efficient two-hybrid selection in yeast. *Genetics*. 144:1425–1436.

Kabsch, W. 2010. Xds. *Acta Crystallogr. D Biol. Crystallogr.* 66:125–132. http://dx.doi.org/10.1107/S0907444909047337

Kressler, D., E. Hurt, and J. Baβler. 2010. Driving ribosome assembly. *Biochim. Biophys. Acta*. 1803:673–683. http://dx.doi.org/10.1016/j.bbamcr.2009.10.009

Kressler, D., G. Bange, Y. Ogawa, G. Stjepanovic, B. Bradatsch, D. Pratte, S. Amlacher, D. Strauß, Y. Yoneda, J. Katahira, et al. 2012a. Synchronizing nuclear import of ribosomal proteins with ribosome assembly. *Science*. 338:666–671. http://dx.doi.org/10.1126/science.1226960

Kressler, D., E. Hurt, H. Bergler, and J. Bassler. 2012b. The power of AAA-ATPases on the road of pre-60S ribosome maturation—molecular machines that strip pre-ribosomal particles. *Biochim. Biophys. Acta*. 1823:92–100. http://dx.doi.org/10.1016/j.bbamcr.2011.06.017

Lapeyre, B., and S.K. Purushothaman. 2004. Spb1p-directed formation of Gm2922 in the ribosome catalytic center occurs at a late processing stage. *Mol. Cell*. 16:663–669. http://dx.doi.org/10.1016/j.molcel.2004.10.022

Lebreton, A., C. Saveanu, L. Decourty, A. Jacquier, and M. Fromont-Racine. 2006. Nsa2 is an unstable, conserved factor required for the maturation of 27 SB pre-rRNAs. *J. Biol. Chem.* 281:27099–27108. http://dx.doi.org/10.1074/jbc.M602199200

Lee, W., J.H. Kim, W.M. Westler, and J.L. Markley. 2011. PONDEROSA, an automated 3D-NOESY peak picking program, enables automated protein

structure determination. *Bioinformatics*. 27:1727–1728. http://dx.doi.org/10.1093/bioinformatics/btr200

Leidig, C., M. Thoms, I. Holdermann, B. Bradatsch, O. Berninghausen, G. Bange, I. Sinning, E. Hurt, and R. Beckmann. 2014. 60S ribosome biogenesis requires rotation of the 5S ribonucleoprotein particle. *Nat. Commun.* 5:3491. http://dx.doi.org/10.1038/ncomms4491

Matsuo, Y., S. Granneman, M. Thoms, R.G. Manikas, D. Tollervey, and E. Hurt. 2014. Coupled GTPase and remodelling ATPase activities form a checkpoint for ribosome export. *Nature*. 505:112–116. http://dx.doi.org/10.1038/nature12731

McCoy, A.J., R.W. Grosse-Kunstleve, P.D. Adams, M.D. Winn, L.C. Storoni, and R.J. Read. 2007. Phaser crystallographic software. *J. Appl. Cryst.* 40:658–674. http://dx.doi.org/10.1107/S0021889807021206

Miles, T.D., J. Jakovljevic, E.W. Horsey, P. Harnpicharnchai, L. Tang, and J.L. Woolford Jr. 2005. Ytm1, Nop7, and Erb1 form a complex necessary for maturation of yeast 66S preribosomes. *Mol. Cell. Biol.* 25:10419–10432. http://dx.doi.org/10.1128/MCB.25.23.10419-10432.2005

Moon, A.F., G.A. Mueller, X. Zhong, and L.C. Pedersen. 2010. A synergistic approach to protein crystallization: combination of a fixed-arm carrier with surface entropy reduction. *Protein Sci.* 19:901–913.

Nissan, T.A., J. Bassler, E. Petfalski, D. Tollervey, and E. Hurt. 2002. 60S pre-ribosome formation viewed from assembly in the nucleolus until export to the cytoplasm. *EMBO J.* 21:5539–5547. http://dx.doi.org/10.1093/emboj/cdf547

Nissan, T.A., K. Galani, B. Maco, D. Tollervey, U. Aebi, and E. Hurt. 2004. A pre-ribosome with a tadpole-like structure functions in ATP-dependent maturation of 60S subunits. *Mol. Cell*. 15:295–301. http://dx.doi.org/10.1016/j.molcel.2004.06.033

Orlicky, S., X. Tang, A. Willems, M. Tyers, and F. Sicheri. 2003. Structural basis for phosphodependent substrate selection and orientation by the SCFCdc4 ubiquitin ligase. *Cell*. 112:243–256. http://dx.doi.org/10.1016/S0092-8674(03)00034-5

Rabl, J., M. Leibundgut, S.F. Ataide, A. Haag, and N. Ban. 2011. Crystal structure of the eukaryotic 40S ribosomal subunit in complex with initiation factor 1. *Science*. 331:730–736. http://dx.doi.org/10.1126/science.1198308

Rohrmoser, M., M. Hölzel, T. Grimm, A. Malamoussi, T. Harasim, M. Orban, I. Pfisterer, A. Gruber-Eber, E. Kremmer, and D. Eick. 2007. Interdependence of Pes1, Bop1, and WDR12 controls nucleolar localization and assembly of the PeBoW complex required for maturation of the 60S ribosomal subunit. *Mol. Cell. Biol.* 27:3682–3694. http://dx.doi.org/10.1128/MCB.00172-07

Santos-Rosa, H., H. Moreno, G. Simos, A. Segref, B. Fahrenkrog, N. Panté, and E. Hurt. 1998. Nuclear mRNA export requires complex formation between Mex67p and Mtr2p at the nuclear pores. *Mol. Cell. Biol.* 18:6826–6838.

Sattler, M., J. Schleucher, and C. Griesinger. 1999. Heteronuclear multidimensional NMR experiments for the structure determination of proteins in solution employing pulsed field gradients. *Prog. Nucl. Magn. Reson. Spectrosc.* 34:93–158. http://dx.doi.org/10.1016/S0079-6565(98)00025-9

Sharma, S., J. Yang, P. Watzinger, P. Kötter, and K.D. Entian. 2013. Yeast Nop2 and Rcm1 methylate C2870 and C2278 of the 25S rRNA, respectively. *Nucleic Acids Res.* 41:9062–9076. http://dx.doi.org/10.1093/nar/gkt679

Shen, Y., O. Lange, F. Delaglio, P. Rossi, J.M. Aramini, G. Liu, A. Eletsky, Y. Wu, K.K. Singarapu, A. Lemak, et al. 2008. Consistent blind protein structure generation from NMR chemical shift data. *Proc. Natl. Acad. Sci. USA*. 105:4685–4690. http://dx.doi.org/10.1073/pnas.0800256105

Shen, Y., F. Delaglio, G. Cornilescu, and A. Bax. 2009. TALOS+: a hybrid method for predicting protein backbone torsion angles from NMR chemical shifts. *J. Biomol. NMR*. 44:213–223. http://dx.doi.org/10.1007/s10858-009-9333-z

Stelter, P., and E. Hurt. 2014. A pulse-chase epitope labeling to study cellular dynamics of newly synthesized proteins: a novel strategy to characterize NPC biogenesis and ribosome maturation/export. *Methods Cell Biol.* 122:147–163. http://dx.doi.org/10.1016/B978-0-12-417160-2.00007-2

Stelter, P., R. Kunze, M. Radwan, E. Thomson, K. Thierbach, M. Thoms, and E. Hurt. 2012. Monitoring spatiotemporal biogenesis of macromolecular assemblies by pulse-chase epitope labeling. *Mol. Cell*. 47:788–796. http://dx.doi.org/10.1016/j.molcel.2012.06.015

Strässer, K., J. Bassler, and E. Hurt. 2000. Binding of the Mex67p/Mtr2p heterodimer to FXFG, GLFG, and FG repeat nucleoporins is essential for nuclear mRNA export. *J. Cell Biol.* 150:695–706. http://dx.doi.org/10.1083/jcb.150.4.695

Tang, L., A. Sahasranaman, J. Jakovljevic, E. Schleifman, and J.L. Woolford Jr. 2008. Interactions among Ytm1, Erb1, and Nop7 required for assembly of the Nop7-subcomplex in yeast preribosomes. *Mol. Biol. Cell*. 19:2844–2856. http://dx.doi.org/10.1091/mbc.E07-12-1281

Thomas, B.J., and R. Rothstein. 1989. Elevated recombination rates in transcriptionally active DNA. *Cell*. 56:619–630. http://dx.doi.org/10.1016/0092-8674(89)90584-9

Tschochner, H., and E. Hurt. 2003. Pre-ribosomes on the road from the nucleolus to the cytoplasm. *Trends Cell Biol.* 13:255–263. http://dx.doi.org/10.1016/S0962-8924(03)00054-0

Ulbrich, C., M. Diepholz, J. Bassler, D. Kressler, B. Pertschy, K. Galani, B. Böttcher, and E. Hurt. 2009. Mechanochemical removal of ribosome biogenesis factors from nascent 60S ribosomal subunits. *Cell*. 138:911–922. http://dx.doi.org/10.1016/j.cell.2009.06.045

Woolford, J.L. Jr., and S.J. Baserga. 2013. Ribosome biogenesis in the yeast *Saccharomyces cerevisiae*. *Genetics*. 195:643–681. http://dx.doi.org/10.1534/genetics.113.153197